Synthesis, spectral characterization and biological activities of Ag(I), Pt(IV) and Au(III) complexes with novel azo dye ligand (N,N,O) derived from 2-amino-6-methoxy benzothiazole

Hussein A. K. Kyhoiesh (husseinkyhoiesh@gmail.com)
Republic of Iraq Ministry of Education https://orcid.org/0000-0001-9705-9196
Khalid J. Al-Adilee
University of Al-Qadisiyah

Research Article

Keywords: benzothiazole, MFE-296, Molecular docking, anti-oxidant, anti-microbial, XRD

Posted Date: January 10th, 2022

DOI: https://doi.org/10.21203/rs.3.rs-953144/v1

Version of Record: A version of this preprint was published at Chemical Papers on January 16th, 2022. See the published version at https://doi.org/10.1007/s11696-022-02072-9.

Abstract

The novel ligand 2-[2'-(6-methoxybenzothiazolyl)azo]-3,5-dimethyl benzoic acid (6-MBTAMB), derived from 2-amino-6-methoxy benzothiazole, has been used to synthesize a series of new metal complexes of Ag(I), Pt(IV) and Au(III). The metal complexes were characterized by elemental analyses (CHNS), molar conductivity, crystal structure (XRD), spectroscopic techniques: FT-IR, ^{1}H NMR, ^{13}C NMR, UV-Vis, mass spectra, thermal analysis (TG-DTA), FE-SEM and magnetic properties. Results confirmed that the azo dye ligand behaves a tridentate and coordinates to the metal ion via nitrogen atom of azomethine group of heterocyclic benzothiazole ring, nitrogen atom of the azo group which is the farthest of the benzothiazole molecule and carboxylic oxygen. Antimicrobial properties of all newly synthesized azo compounds are also demonstrated against bacterial pathogenic organisms and fungi. These complexes are more effective against bacteria and less effective against fungi compared to standard antibacterial drugs (Novobiocin) and antifungal drugs (Cycloheximide). By using the DPPH (2,2-diphenyl-1-picrylhydrazyl) radical scavenging test, it was discovered that the complexes had good antioxidant properties. In addition, the (6-MBTAMB) and metal complexes were docked with the crystal structure of FGF Receptor 2 (FGFR2) kinase domain harboring the pathogenic gain of function K659E mutation identified in endometrial cancer using the Molecular Operating Environment module (MOE). In vitro studies on human endometrial cancer cell lines (MFE-296) as well as healthy human umbilical vein endothelial cells (HUVEC) show uptake of the intact compounds by the cancer cells and increased activity against the cancer cells.

Highlight

- Diazo-coupling was used to synthesize the heterocyclic azo dye ligand (6-MBTAMB).
- Newly synthesized azo compounds have been confirmed by various spectroscopic techniques.
- Antimicrobial, antioxidant, anticancer, and molecular docking were used to evaluate 6-MBTAMB with metal complexes.
- MFE-296 cells were more responsive to 6-MBTAMB and Au(III)-Complex
- Cytotoxicity with IC_{50} of 6-MBTAMB is 100.4 µg/ml and Au(III) metal complex is 43.44 µg/ml in MFE-296 cell line.

1. Introduction

Medicinal chemists are interested in benzothiazole derivatives because of their diverse biological functions, which include anti-inflammatory (Venkatesh and Pandeya 2009), analgesic (Verma, Martin, and Singh Sr 2014), antibacterial (Tang et al. 2019), and antiviral (Kaur et al. 2010). Marine and terrestrial natural compounds with valuable biological functions contain the benzothiazole ring system (Prajapat 2012). 2-aminobenzothiazoles are extremely reactive compounds and are widely used as reactants or intermediates since the roles of NH_2 and endocyclic N are suitable for reactions with different reactants to form a variety of fusing heterocyclic compounds (Dadmal et al. 2018). Several heterocyclic derivatives of nitrogen and sulfur atoms are used in experimental drug design to serve as special and versatile scaffolding (Singh and Singh 2014).

The benzothiazole molecule consists of a thiazole ring fused to a benzene ring. In the 1950s, the chemical family of 2-aminobenzothiazoles was extensively investigated as muscle relaxants. Biologists became interested in this sequence when it was discovered that glutamate neurotransmission inhibitors also occur in Riluzole (6-trifluoromethoxy -2-benzothiazolamines). According to its diversified molecular nature and extraordinary optical, liquid, and electronic properties, benzothiazole has received an overwhelming response (Khokra et al. 2011; Bhat and Belagali 2014; Ha et al. 2009). In the manufacturing of such dispersed azo coloring 2-aminobenzothiazole is used. For the prevention of amyotrophic lateral sclerosis (Mignani et al. 2020) and 2-(4-aminophenyl)benzothiazole proof of antitumor properties (Mavroidi et al. 2016), riluzole (2-amino-6-trifluoromethoxybenzothiazole) is sold as an anti-tumour (Araki et al. 2001). The benzothiazole derivative catalyzes the formation of sulfide links (reticulation) among unsaturated elastomeric polymers to obtain a flexible and elastic crosslinking material (Ibrahim, Arafa, and Behbehani 2018). Rubber accelerators such as 2-mercaptobenzothiazole (MBT/BTSH) are widely used in a variety of products including tire manufacturing (Vernack et al. 2020).

Metallodrugs have become a key component of medicinal chemistry in the past few years. Many important factors must be considered before the synthesis of complexes used for medicinal purposes, including the choice of metal ions, their oxidation state, their stability, and the choice of inert and labile ligands. As a result, many compounds of transition metal ions have found application as diagnostic and therapeutic agents (Radisavljević and Petrović 2020). However, gold compounds have attracted the most attention. Various gold compounds have been used to treat cancer, HIV, rheumatoid arthritis (chrysotherapy), and other diseases (Stankovic et al. 2019; Sun et al. 2021; Currie 2018). This metal ion has unoccupied d-sublevels and is possible to form compounds with a wide range of oxidation states, between -1 to $^{+}5$. Chemically, gold(I) and gold(III) complexes are dominant. Especially gold(III) complexes are of great interest since they resemble cisplatin structurally (da Silva Maia, Deflon, and Abram 2014; Milacic and Dou 2009).

The spectral, chemical and electrochemical properties of transition metal complexes have inspired extensive research into their potential use as anticancer drugs (Sun et al. 2007). Chemistry biology is currently focused on the study of the interaction of metal complexes with DNA (Wang et al. 2011). In clinical trials, platinum-based medications have been used for over 30 years. Patients undergoing chemotherapy commonly receive platinum-based medications, such as cis-platin, which bind covalently to DNA bases. However, there are several limitations to the potency of cis-platin, such as increased tumor tolerances and high toxicity. In order to overcome these limitations, small molecules have been explored and synthesized that interact with DNA in a sequence-specific manner. Transition metal complexes, rather than platinum related compounds, are in use as medicine for treating some tumors, diagnosing diseases, and validating DNA sequences (Boulikas and Vougiouka 2003; Sirajuddin and Ali 2016). Biologically, silver and gold are important transition metal ions because they function as essential biochemical traces (D'ulivo, Lampugnani, and Zamboni 1991).

The present study describes the synthesis and characterization of a new heterocyclic azo dye ligand (6-MBTAMB) with Ag(I), Pt(IV) and Au(III) metal complexes, along with their antioxidant, antimicrobial and anticancer activities. Molecular docking was used to determine how effective these compounds are

against cancer. (6-MBTAMB) and Au(III)-Complex were examined for cytotoxicity in endometrial cancer (MFE-296), human umbilical vein endothelial cells (HUVEC). Further investigation of structure is guided by elemental analyses (C.H.N.S), FT-IR, ^{1}H & ^{13}C-NMR, UV-Vis, thermal stability (TGA/DTA), crystal structure (XRD), FE-SEM, magnetic moment and molar conductance.

2. Experimental

2.1. Chemicals and reagent

Synthesized materials were analytical reagent grade chemicals and solvents, and their purification was not required. Provided excellent chemicals such as 2-amino-6-methoxy benzothiazole, 3,5-dimethyl benzoic acid, 1,1-diphenyl-2-picrylhydrazyl (DPPH), 3-(4,5-dimethylthiazol-2-yl)-2,5-diphenyltetrazolium bromide (MTT), ascorbic acid, $NaNO_2$, $AgNO_3$, $H_2PtCl_6.6H_2O$, $HAuCl_4.4H_2O$, HCl, NaOH, DMSO, DMF, absolute EtOH, MeOH, K_2CO_3, K_2CrO_4, CO_2, $CaCl_2$, Silica Gel 60, Deionized water, foetal bovine serum (FBS), Novobiocin, Cycloheximide. In addition, MS (mannitol salt) and potato dextrose (PDA) agars were purchased from commercial suppliers (B.H.D (England), Sigma-Aldrich (Germany), Honeywell Fluka (UK), Merck (Germany), Scharlu (España), FUJIFILM Wako Pure Chemical Corporation (Japan), J&K chemical (China), Alfa Acer (U.S), S. D. Fine-Chem Limited (India) and others.

2.2. Physical measurements

Microelement analyses (carbon, nitrogen, hydrogen and sulfur) of ligand and its metal complexes were performed on an element analyzer (EA 300, C.H.N.S.). Atomic absorption spectroscopy was used to determine the metal contents of the Ag(I), Pt(IV) and Au(III) complexes. The molar conductance of DMF and absolute ethanol solutions (10^{-3} mol L^{-1}) were measured at room temperature (25±0.01°C) using a 31 A digital conductivity bridge. Spectra of the ^{1}H and ^{13}C NMR were obtained on a Bruker 500 MHZ spectrometer using DMSO-d_6 as a solvent and TMS as an internal reference. FT-IR spectra (KBr disks, 4000–400 cm^{-1}) were recorded using an 8400 S from Shimadzu. In absolute ethanol using a quartz cuvette of 1 cm path length, the electronic spectra of samples were measured on a T80-PG double beam (UV-Vis) spectrophotometer in the range of 200-1100 nm. A magnetic susceptibility balance model (MSB/MKIC) was used for magnetic measurements. Pascal's constants and diamagnetic corrections were derived from the values given by Selwood (French 1944). Magnetic moments were calculated using the equation (Bain and Berry 2008; Ding and Zheng 2021), μeff=2.84 $[T\chi M^{coor}]^{1/2}$. Using a Shimadzu Agilent Technologies 5973C (70 eV) mass spectrometer, mass spectra were recorded for the ligand (6-MBTAMB) and Au(III). Thermal analysis (TGA-DTA) were investigated with a PL-TG instrument from 25 to 900°C under a nitrogen atmosphere with a heating rate of (10°C min^{-1}), in the temperature range from 25 to 900°C. X-ray diffraction (XRD) measurements were conducted in the range of (20-80°)2Θ using an aluminum anode-Germany X-ray diffractometer with (Cu Kα) radiation (λ = 1.5418 °A). Voltage and current in the X-ray tube were 40 kV and 25 mA, respectively. Field emission scanning electron microscopy (FESEM) was used to obtain morphological images using a ZEISS EM 3200. For recording melting points or decomposition temperatures, the Stuart instrument was applied. The pH meter measurements were performed with a Philips PW 9421 (±0.001). Chem Draw software was used to design the compounds, which were then optimized via ChemBio3D software.

2.3. Synthesis of Azo Ligand 2-[2'-(6-Methoxy Benzothiazolyl)azo]-3,5-Dimethyl Benzoic Acid (6-MBTAMB)

Our laboratory prepared ligand (6-MBTAMB) based on the work done by Al-Adilee and his group with a few modifications to the procedure (Al-Adilee, Abedalrazaq, and Al-Hamdiny 2013; Al-Adilee and Kyhoiesh 2017; Harisha et al. 2020). The ligand (6-MBTAMB) for benzothiazolyl azo dye was synthesized in two steps. In the first step, 2-amino-6-methoxy benzothiazole (1.80 g, $1.00x10^{-3}$ mol) was dissolved in a mixture of 5 mL hydrochloric acid (HCl) and 30 mL distilled water (H_2O). Components were diazotized below 0-5°C with a cold solution of $NaNO_2$ (1.00 g, $1.00x10^{-3}$ mol) and 35 ml distilled H_2O) with cooling was applied drop-wise. For in the second step, the diazonium salt compound was coupled with (1.24 g, $1.00x10^{-3}$ mol) 3,5-dimethyl benzoic acid was dissolved in 40 mL of ethanol in alkaline media from 12 mL of 15% NaOH and 5 ml K_2CO_3 for coupling after the mixture had been stirring for 1 hour below 0°C. After that, the mixture was stirred in an ice bath and filtered, then the precipitate was washed several times with distilled water, purified with absolute ethanol solution by recrystallization, and dried for a few hours in the oven at 50°C. The purity of the azo dye ligand is determined by TLC using silica gel G (R_f = 0.9).

2.4. Synthesis of the complexes

The metal complexes were made from dissolving (0.341 g, $1.00x10^{-3}$ mol) from the ligand (6-MBTAMB) in hot ethanol (50 mL). In a stoichiometric ratio of 1: 1 [M: L] with (0.170 g, $1.00x10^{-3}$ mol) of $AgNO_3$, add the solution dropwise with stirring, (0.410 g, $1.00x10^{-3}$ mol) of $H_2PtCl_6.6H_2O$, (0.518 g, $1.00x10^{-3}$ mol) of $HAuCl_4.4H_2O$. For each metal ion, a buffer solution (ammonium acetate) was dissolved in the little quantity required, while platinum (IV) salt was dissolved in a methanol solution with drops of hydrochloric acid. Refluxing the reaction mixture for 60 minutes, it was then left overnight. Solid complexes were filtered off, washed with distilled water and little warm ethanol to remove any unreacted components. Several hours at 60 ^{o}C were spent drying the solid complexes in a desiccator over anhydrous $CaCl_2$. Table 1 includes analytical data on C, H, N, and S as well as the physical properties of complexes.

2.5. Antimicrobial study (in vitro)

The antimicrobial evaluation of the investigated samples was performed using the agar diffusion method (Chiu et al. 2021; Roy et al. 2021). Two different species of (Gram-positive) and (Gram-negative) bacteria were examined using the sensitivity test system to determine whether the compounds had inhibitory effects. In vitro antibacterial activity of the synthesized ligands and their metal complexes was examined against bacterial species including *Staphylococcus aureus* (MTCC 3160) and *Escherichia coli* (MTCC 723). Additionally, the antifungal agents were tested on *Aspergillus niger* (MTCC 1881). During the experiments, bacteria and fungi were housed on nutrient agar medium and potato dextrose (PDA), respectively. Different test microorganisms were inoculated into the agar media. Gram's method has also been used to diagnose bacteria (Hillier 1993). Microbial growth was determined by measuring the diameter zone

of inhibition with the help of scale. The diameter of the inhibitory zone was measured after 24 hours and 7 days, in the (DMSO) solvent, for bacteria and fungi, respectively. Each solution contained 0.2 mg/mL of DMSO by the agar well diffusion method. The antibacterial drug was (Novobiocin), and the antifungal drug was (Cycloheximide). DMSO served as a negative and positive control.

2.6. Molecular docking

The Molecular Operating Environment module (MOE) was used to perform the biological evaluation (cytotoxic and antioxidant) of the ligand (6-MBTAMB) and metal complexes using the crystal structure of FGF Receptor 2 (FGFR2) kinase domain harboring the pathogenic gain of function K659E mutation identified in endometrial cancer (Chen et al. 2013). A crystal structure of protein FGFR2 (PDB ID: 4J97) is available in the protein data bank (PDB) (http://www.rcsb.org) (Bank-tiedosto 2000). MOE 2014 was used to create 3D structures, add charges, minimize energy, and gather all structures in one molecular database file. Amino acids were preserved, and water molecules and crystallized ligands were eliminated. 6-MBTAMB and chelate complexes were designed and optimized using the ChemBio Ultra software (16.0, Cambridge Soft) and Gaussian software, respectively. Finally, docking experiments were conducted using MOE 2014 docking wizard with induced fit as docking protocol, triangle match for placement, force field refinement for docking refinement, and affinity DG for the initial scoring and London DG for the final score (Sulimov et al. 2021; Harris et al. 2014).

2.7. Antioxidant assay (free radical scavenging activity)

The 2,2-diphenyl-1-picrylhydrazyl (DPPH) method was used to test antioxidant activity. Different concentrations (12.5, 25, 50, 100, 200 and 400 µg/ml) of samples in methanol. 0.3 ml of different concentration solutions were prepared and mixed with 2.7 ml of a methanol solution containing DPPH radicals. Using a UV-Vis spectrophotometer, the absorbance at 517 nm was measured to determine the amount of DPPH radical scavenged. The mixture was shaken well and left at room temperature for 60 minutes. The means for each concentration are determined by three independent replications. The antioxidant capacity was calculated using ascorbic acid as a standard (positive control). Radical scavenging activity was calculated using the following formula (İnci, Aydın, and Zorlu 2021; Kyhoiesh et al. 2021); %Radical scavenging activity = [(Control OD-Sample OD)/Control OD)]×100, where (Control OD) is the absorbance of the control reaction (containing all reagents except the test compound) and (Sample OD) is the absorbance of the test compound. Calculated IC_{50} values for synthesized compounds and standard preparation are obtained by plotting DPPH-scavenging activity against sample concentration.

2.8. Cytotoxic studies-MTT assay

Cytotoxicity tests were performed on novel benzothiazolyl azo ligand (6-MBTAMB) and Au(III)-Complex against human endometrial cancer cell lines (MFE-296) and normal human umbilical vein endothelial cells (HUVEC) (Loffredo et al. 2021). Cell lines were purchased from the Iranian Biological Resource Center (IBRC; Tehran, Iran). The modified cell viability (MTT) method was applied to perform this assessment, and MTT (3-[4,5-dimethylthiazolyl]-2,5-diphenyltetrazolium bromide) reduction was determined using the method indicated above (Kumar, Nagarajan, and Uchil 2018). For 24 hours, cells were seeded at a density of $1*10^5$ cells/well in 96-well clear flat-bottom plates (Greiner Bio-One, Frickenhausen, Germany). The medium was extracted after 24 hours of incubation at 37°C, and the cells were treated with synthesized compounds (0, 25, 50, 100, 200 and 400 µg/ml). After a 48-hour incubation period at 37°C, the medium was withdrawn from the plate. Every well was then filled with 200 µl of MTT reagent (1 mg/ml) in a serum-free medium. The medium was extracted after 4 hours, and 200 µl (DMSO) was applied to each well. The absorbance of the metabolized MTT agent dissolved in DMSO was measured using a microplate reader at a wavelength of 570 nm. Triplicate tests were performed at each concentration. Measurement of optical density (OD) was performed on each well using an ELISA plate reader (infinite F50, TECAN, Austria). The % cell viability was calculated as (mean OD of treated cells/mean OD of untreated cells) x100 (Marks et al. 1992; Gasparini et al. 2017). The 50% inhibitory concentration (IC_{50}) values were measured and the IC_{50} curves were plotted using a sigmoidal dose-response equation.

2.9. Statistical analysis

The experiments were conducted as many times as possible, in triplicates and on different occasions. The outcomes are reported as mean ± standard deviation (S.D). Standard curves and 50% inhibitory concentrations (IC_{50}) were calculated using GraphPad Prism Version 9.0.2 (La Jolla, CA, USA) for Windows (GraphPad Software Inc.) (Choueiry et al. 2021). Cytotoxicity is determined by the percentage of cells that survive compared to untreated controls.

3. Results And Discussion

3.1. Physical and chemical properties of azo ligand (6-MBTAMB) and chelate complexes

The synthesized azo dye ligand (6-MBTAMB) and its complexes are very stable at room temperature in the solid state, insoluble water, but soluble in dimethyl sulfoxide (DMSO), dimethylformamide (DMF), ethanol (EtOH), methanol (MeOH), Acetone $(CH_3)_2CO$ and formic acid (HCOOH). The yields, melting points, pH, colors, elemental analyses (CHNS) of azo dye ligand and its metals complexes are presented in Table 1. The analytical results are well consistent with the proposed stoichiometry of the complexes. FT-IR and resonance signals in ^1H NMR and ^{13}C NMR spectra provided information about the formation of azo dye ligand (6-MBTAMB) and its metal complexes. The geometry around Ag(I), Pt(IV) and Au(III) ions in the complexes was deduced from the positions of absorption bands observed in the electronic spectra and magnetic moment values. The crystallite size, parameters and morphology have been estimated using XRD and FE-SEM analysis, respectively.

3.2. Metal:Ligand Ratio

This method was introduced by Yoe and Jones (Watarai and Chen 2017; Al-Adilee and Waheeb 2020). A series of solutions are prepared in which the total concentration of the metal is kept constant and the concentration of the ligand is varied under similar conditions. A plot is prepared of absorbance as a function of the ratio of moles of ligand to moles of the metal (Meyer Jr and Ayres 1957). For the complexes, a curve with a positive slope is obtained till mole

ratio value one after which there is no increase. This indicates that metal has been used up entirely at mole ratio one and further addition of ligand (6-MBTAMB) produce no more complexation. Molar ratio data revealed that the ligand to metal ratio was 1:1 for Ag(I), Pt(IV) and Au(III) chelate complexes.

3.3. Molar conductivity

Conductivity changes can frequently be useful for studying the reactions of metal complexes in solution. Molar conductivities (Λ_M) are normally determined using (1.00×10^{-3} M) solutions of the complexes (Liu et al. 2006; Ahmed, Atta, and Refat 2014). According to Table 1, the molar conductance measurements of Ag (I) and Pt (IV) complexes in EtOH and DMF solutions are low (13.15-28.19 $S.cm^2. mol^{-1}$), suggesting that the complexes are not electrolytes (Gao et al. 1995). For Au(III) metal complex, EtOH and DMF conductivity values are 41.91 and 77.24 $S.cm^2. mol^{-1}$, respectively. Based on the Mohr Method (Berger and Dawson 1952), the presence or absence of chloride (counter) ions can be determined. In addition, the presence of white precipitate of Au(III) metal complex indicates an electrolytic nature (1:1) electrolyte of the complex, and the chloride ion is outside the coordination sphere. Table 1 shows the molar conductance (Λ_m) values of the complexes are dissolved in DMF and EtOH.

Table 1
Physical properties and analytical data for ligand (6-MBTAMB) and its metal complexes.

Compound	Color	m.p °C	pH	Yield%	Molecular Formula (M.wt) (g/mol)	Found% (Calculated)					Molar conductivity $S.cm^2. mol^{-1}$	
						C%	H%	%N	%S	%M	DMF	EtOH
6-MBTAMB	Dark brown	168	6.5	80	$C_{17}H_{15}N_3O_3S$ (341.38)	59.83 (59.81)	4.40 (4.43)	12.42 (12.31)	9.35 (9.39)	—	—	—
[Ag(L)(H_2O)].H_2O	Pale brown	176	7.7	68	$C_{17}H_{18}N_3O_5SAg$ 484.27))	42.22 (42.16)	3.76 (3.75)	8.70 (8.68)	6.68 (6.62)	22.30 (22.27)	24.90	18.32
[Pt(L)Cl_3].H_2O	Umber	191	7.5	59	$C_{17}H_{16}N_3O_4SCl_3Pt$ 659.83))	31.00 (30.94)	2.46 (2.44)	6.39 (6.37)	4.95 (4.86)	29.68 (29.56)	28.19	13.15
[Au(L)Cl]Cl.H_2O	Yellowish orange	170	7.5	65	$C_{17}H_{16}N_3O_4SCl_2Au$ 626.26))	31.88 (31.79)	2.59 (2.51)	6.60 (6.54)	5.13 (4.99)	30.80 (30.67)	77.24	41.91

m.p = melting point.

3.4. ^{1}H NMR Spectra

The ^{1}H NMR spectral results, obtained for azo dye ligand (6-MBTAMB) and Au(III) complex at room temperature in DMSO-d6 with TMS as an internal reference (500 MHZ) (Jaber, Kyhoiesh, and Jawad 2021). The spectrum of free ligand (6-MBTAMB) display a signal at (δ = 9.33-9.35) ppm (1H, s, 24) due to the presence of carboxylate group, and the disappearance of the (-COOH) signal in the ^{1}H NMR spectra of Au(III) complex can be attributed to the break of the hydrogen bond as the result of metal chelation. (Figures 1, 2, and Table 2) shows that the bands observed at (δ = 7.07-7.99) ppm and (δ = 6.93-7.75) ppm (5H,d,m,dd,m,7,9,17,19,6) are assigned to the aromatic protons (benzothiazole ring and phenyl ring) of the (6-MBTAMB) and its Au(III) complex, respectively. The ligand (6-MBTAMB) exhibited signals of (δ = 3.82-3.89) ppm (3H,s,11), (δ = 2.53) ppm (3H,s,20) and (δ = 2.47) ppm (3H,s,21) that belonged to (-OCH_3) and CH_3 groups, a signal at (δ = 2.51) ppm (s, solvent proton). On the other hand, ^{1}H NMR spectra of Au (III) metal complex displayed signals of (δ = 3.72-3.89) ppm (3H,s,11), (δ = 2.53) ppm (3H,s,20) and (δ = 2.28) ppm (3H,s,21) that assigned to (-OCH_3) and CH_3 groups, a signal at (δ = 2.51) ppm (s, solvent proton).

Upon coordination, ^{1}H NMR signals from (-COOH) disappeared from other complexes, which indicated that the carboxylate group was deprotonated as a result of M-O bonds forming, as the signal intensity and location changed in comparison with ligand spectra (Al-Saif 2014).

Table 2

^{1}H NMR spectra of ligand (6-MBTAMB) and its Au(III)-Complex.

6-MBTAMB	J-J	Associated group	Au(III)-Complex	J-J	Associated group
δ, ppm, (H atoms, peak, assignment)	Coupling		*δ*, ppm, (H atoms, peak, assignment)	Coupling	
2.51 (DMSO-d_6)	*12.15*	*Solvent*	*2.51 (DMSO-d_6)*	*6.70*	*Solvent*
2.47 (3H,S,21)	*3.15*	*-CH_3*	*2.28 (3H,S,21)*	*3.77*	*-CH_3*
2.53 (3H,S,20)	*3.31*	*-CH_3*	*2.53 (3H,S,20)*	*3.38*	*-CH_3*
3.82-3.89 (3H,S,11)	*2.61*	*-OCH_3*	*3.72-3.89 (3H,S,11)*	*2.99*	*-OCH_3*
7.07-7.99 (5H,d,m,dd,m,7,9,17,19,6)	*1.45,0.90,3.11*	*-Ar-H, -benzo-H*	*6.93-7.75 (5H,d,m,dd,m,7,9,17,19,6)*	*3.20,1.17*	*-Ar-H, -benzo-H*
9.33-9.35 (1H,S,24)	*0.79*	*-COOH*	*Coordinated*	*-*	*-COOH*
s= singlet, d= doublet, dd= doublet-doublet, m= multiplets					

3.5. ^{13}C NMR spectra

The ^{13}C NMR of the ligand (6-MBTAMB) was investigated, and signals were observed due to the presence of various carbon atom types (Pestov et al. 2015). The ^{13}C NMR spectrum showed multiple chemical shifts ^{13}C = (168.69, 159.22, 157.76, 142.19, 139.77, 132.63, 131.01, 127.81, 126.86, 115.61, 113.38, 112.68, 110.12, 106.29, 56.16 and 21.79 ppm) to the carbon atoms at the positions (C_{22}, C_2, C_8, C_4, C_{18}, C_{14}, C_{19}, C_5, C_{15}, C_6, C_7, C_9, C_{16}, C_{17}, C_{11}, C_{20}, C_{21}), respectively. The spectrum also showed a singlet signals of Au(III) metal complex at the chemical shift ^{13}C = (168.97, 159.52, 143.42, 142.17, 139.76, 139.60, 133.07, 132.63, 131.00, 127.85, 126.85, 113.20, 109.59, 106.00, 56.03, 21.79 and 21.28 ppm) to carbon atoms at the same ligand positions by changing chemical displacements (Waheeb and Al-Adilee 2021). ^{13}C NMR spectrum of the ligand (6-MBTAMB) and Au(III)-Complex are presented in Figures 3 and 4.

3.6. Mass Spectral Analysis

The mass spectrum can be used to verify both the structure and the complexes of the ligand. The fragmentation ligand (6-MBTAMB) and Au(III)-complex mass spectrum showed multiple peaks (Schemes 1 and 2). The detailed mass spectral data have been tabulated in (Table 3). The mass spectral of the new benzothiazolyl azo ligand reveals a base peak at m/z^{+}=341.7, base peak (64.03%) attributed to the molecular weight of the ligand (6-MBTAMB) (341.38), [$C_{17}H_{15}N_3O_3S$]. The molecular peak of Au(III)-Complex that appeared in m/z^{+}= 625.6, base peak (3.30%) is corresponding to the molecular formula of complex (626.26), [$C_{17}H_{16}N_3O_4SAuCl_2$]. This data is a good agreement with the corresponding molecular formulae (Chandra and Gupta 2005; AL-Adilee, Abass, and Taher 2016; Habeeb, Al-Adilee, and Jaber 2014). Consequently, the results of mass spectrometry and elemental analysis support the formation of stoichiometric complexes. Figures 5 and 6 show patterns of azo dye ligand (6-MBTAMB) and Au(III)-Complex.

Table 3
Suggested mass fragment products for (6-MBTAMB) and Au(III)-Complex.

6-MBTAMB			Au(III)-Complex		
m/z+	Exact mass Fragment	Base Peak %	m/z+	Exact mass Fragment	Base Peak %
341.70	$[C_{17}H_{15}N_3O_3S]$	64.03	625.6	$[C_{17}H_{16}N_3O_4SAuCl_2]$	3.30
328	$[C_{16}H_{14}N_3O_3S]^+$	100.00	562	$[C_{16}H_{13}N_3OSAuCl_2].^+$	2.08
313	$[C_{15}H_{14}N_3O_3S].^+$	79.56	367	$[C_{16}H_{15}N_3OSAuCl_2]$	6.66
298	$[C_{15}H_{12}N_3O_2S]^+$	40.36	316	$[C_{13}H_{14}N_3O_3SAu]^+$	7.73
285	$[C_{14}H_{11}N_3O_2S].^+$	36.83	299	$[C_{16}H_{15}N_3OS]^+$	6.18
269	$[C_{14}H_{11}N_3OS]$ $[C_{14}H_{11}N_3OS].^+$	30.03	284	$[C_{15}H_{14}N_3OS]^+$	4.21
254	$[C_{13}H_8N_3OS]^+$	12.61	256	$[C_{15}H_{14}NOS]^+$	6.83
241	$[C_{13}H_{11}N_3S]$	12.82	210	$[C_{13}H_8NS]^+$	6.67
180	$[C_8H_6NO_2S]^+$	36.12	180	$[C_8H_6NO_2S]^+$	5.55
164	$[C_8H_6NOS]^+$	25.54	164	$[C_8H_6NOS]^+$	5.14
149	$[C_8H_7NS]$	28.82	149	$[C_8H_7NS]$ $[C_7H_3NOS].^+$	40.55
137	$[C_7H_7NS]$	26.37	134	$[C_7H_4NS].^+$	23.54
134	$[C_4H_8NO_2S]$	8.01	133	$[C_7H_4NS].^+$	5.30
120	$[C_7H_4S].^+$	20.89	94	$[C_6H_9N]^+$	15.24
110	$[C_6H_6S]^+$	6.72	77	$[C_6H_5]^+$	40.59
109	$[C_6H_5S]^+$	12.95	69	$[C_5H_9]^+$	100.00
108	$[C_6H_4S].^+$	14.26	64	$[C_5H_4]^+$	7.41
85	$[C_3H_3NS]$	11.84	52	$[C_4H_4]$	9.71
80	$[C_6H_8]$	18.71			
69	$[C_5H_9]^+$	28.34			
64	$[C_5H_4].^+$	8.85			
57	$[C_3H_7N]$	23.79			
53	$[C_4H_5]^+$	4.79			

3.7. Infrared spectra

Infrared spectra of the ligand (6-MBTAMB) and its complexes with Ag(I), Pt(IV) and Au(III) ions have been studied. Complexity in these spectra is attributed to bands formed by benzothiazole and phenyl rings overlapping with other bands arising from υ(C=N), υ(N=N) and υ(COO-). The differences between the bands of complexes and the bands of ligand absorption suggest possible bonds between the complexes. Two characteristic absorption bands in the ranges (1566-1542 cm^{-1}) and (1404-1380 cm^{-1}) were observed which can be attributed to asymmetric and symmetric υ(COO) stretching vibrations, respectively. The carboxylate group can bind to the metal ions in a monodentate, bidentate, or bridging manner. The frequency difference [$\Delta\upsilon = \upsilon(COO^-)_{asym} - \upsilon(COO\text{-})_{sym}$] can be used as an indication of the binding mode of the carboxylate. If Δυ is greater than 162 cm^{-1}, this group is probably bound in a monodentate way, as was observed for the complexes (Soliman and Mohamed 2013).

The spectrum of (6-MBTAMB) shows a broad weak band around 3441 cm^{-1} due to the presence of (O-H) in the carboxyl group. It indicates hydrogen bonding between molecules. Water molecules can be observed in the spectra of Ag(I), Pt(IV) and Au(III) complexes as broad weak to strong absorption bands at 3394-3479 cm^{-1}. The weak bands observed in the 6-MBTAMB spectrum at 3055 cm^{-1} and 2970 cm^{-1} were attributed to $\upsilon(C\text{-}H)_{aromatic}$ and $\upsilon(C\text{-}H)_{aliphatic}$, respectively. These bands are shifted in both ligand (6-MBTAMB) and metal complexes. Spectroscopically, the 6-MBTAMB exhibits absorption at 1697 cm^{-1} and 1625 cm^{-1} as a result of absorption caused by the υ(C=O) and υ(C=N), respectively. In the produced complexes spectra, these bands alter in shape and shift to lower wavenumbers (1682-1605) cm^{-1} indicated metal coordination with nitrogen in the benzothiazole ring (Sagdinc et al. 2009). As can be seen in the spectrum of free ligand, strong band at 1497 cm^{-1} attributed to υ(N=N) stretching, because of the complexity associated with metal ions, this band is changing to a lower frequency and reduced in intensity (Tamer et al. 2020). In addition, the spectrum shows the band at 1266 cm^{-1}, which correspond to the υ(C-S) of the benzothiazole ring. Spectra of ligands and solid chelate complexes exhibit the same band, indicating the non-participation of in complexes formation (Al-Adilee and Hesson 2015). Further weak bands can be seen in the spectrum of complexes in (520– 417) cm^{-1}, which were not present in the ligand spectrum. These bands are assigned to υ(M-O), υ(M-N) and υ(M-Cl). The FT-IR spectra results show that the reagent acts as a tridentate chelating agent, oxygen from the carboxyl group, azo nitrogen, and nitrogen in the benzothiazole ring producing a five and six members chelating ring that coordinates with metal ions. The spectra of the (6-MBTAMB) and its complexes are shown in Figure 7 and Table 4.

Table 4
FT-IR spectra bands of the (6-MBTAMB) and its metal complexes in cm^{-1} units.

Group	6-MBTAMB	Ag(I)-Complex	Pt(IV)-Complex	Au(III)-Complex
$\upsilon(O\text{-}H)\ \upsilon(H_2O)$	3441 w.br.	*3425 s. br.	*3479 s. br.	*3394 m. br.
$\upsilon(C\text{-}H)_{Aromatic}$	3055 w.	3032 w.	2978 w.	2901 w.
$\upsilon(C\text{-}H)_{Aliphatic}$	2970 w.	2924 w.	2885 w.	2831 w.
υ(C=O)	1697 s.	1651 w.	1682 m.	1682 m.
υ(C=N)	1625 m.	1612 w.	1612 w.	1605 m.
$\upsilon(COO\text{-})_{asym}$	1566 m.	1543 m.	1543 w.	1558 m.
υ(N=N)	1497 w.	1450 w.	1459 w.	1459 w.
$\upsilon(COO\text{-})_{sym}$	1404 w.	1381 s.	1404 w.	1396 s.
$\Delta\upsilon(\upsilon(COO\text{-})_{asym}\text{-}\upsilon(COO\text{-})_{sym})$	162	162	139	162
υ(C=C)	1312 w.	1312 w.	1312 w.	1312 w.
	717 w.	795 w.	771 w.	771 w.
υ(C-S)	1265 m.	1265 w.	1273 m.	1265 m.
	833 w.	825 w.	803 w.	833 w.
υ(C-O)	1234 m.	1227 w.	1234 w.	1219 m.
υ(C-N)	1057 w.	1057 w.	1057 w.	1057 w.
υ(C-C)	1026 w.	1026 w.	1026 w.	1026 w.
$\upsilon(M\text{-}OH_2)$	-	648 w.	-	-
υ(M-O)	-	517 w.	520 w.	517 w.
υ(M-N)	-	440 w.	440 w.	440 w.
υ(M-Cl)	-	-	417 w.	417 w.
Ligand (6-MBTAMB), Vs = very strong, S = strong, m = medium, w = weak, br = broad, sh = sharp, as=asymmetric, s=symmetric, * = (H_2O) outside of sphere coordination.				

3.8. Electronic spectral and Magnetic moment studies

The electronic absorption spectral data (λ_{max}, nm) and room temperature magnetic moment values (μ_{eff} B.M.) are essential for proposing the stereochemistry or geometry of the metal complexes. The UV-Vis spectra of 10^{-4} M solution of free ligand (6-MBTANB) and its complexes in absolute ethanol at room temperature are given in Figure 8 and Table 5. The electronic spectrum for ligand (6-MBTAMB) showed three peaks at 434 nm (23041 cm^{-1}), 312 nm (32051 cm^{-1}) and 242 nm (41322 cm^{-1}). The first band can be assigned to $n \rightarrow \pi^*$ intermolecular transition charge transfer taking place through the azo group and azomethine group. While the second and third bands are due to the $\pi \rightarrow \pi^*$ transition of the aromatic benzene ring, chromophores (COOH) and allowed the transition of the benzothiazole ring. In comparison to the free ligand spectrum, the complex solution spectrum showed a significant bathochromic shift in the visible region of the spectrum (Christensson et al. 2013; Chu, Medvetz, and Pang 2007). The electronic spectra of the Ag(I) complex do not exhibit any d-d transition due to electron saturation d^{10}. The absorption bands 446 nm (22422 cm^{-1}), 362 nm (27624 cm^{-1}), 326 nm (30675 cm^{-1}) and 240 nm (41667 cm^{-1})

could be attributed to the presence of a charge transfer dπ(Ag)$^{+1}$→ π*(L)(C.T) and intra ligand. Where π*(L) was believed to be primarily dominated by the LUMO of the azoimine chromosphere (Al-Adilee and Jaber 2018). The magnetic susceptibility shows that this complex has a diamagnetic moment (μ_{eff} = 0.0 B.M) and a tetrahedral geometry (hybridization sp^3). The Pt(IV) complex exhibits bands in the UV-Vis spectra at 486 nm (20576 cm^{-1}), 380 nm (26316 cm^{-1}) and 264 nm (37879 cm^{-1}) which assigned to the transitions $^1A_1g \rightarrow {}^1T_1g_{(F)}(\upsilon_1)$, $^1A_1g \rightarrow {}^1T_2g_{(F)}(\upsilon_2)$ and $^1A_1g \rightarrow {}^1T_1g_{(p)}(\upsilon_3)$ transition (Jovanović, Petrović, and Bugarčić 2010). The complex has diamagnetic behaviour, an octahedral geometry (hybridization d^2sp^3) around Pt(IV) can be suggested. The spectra of the diamagnetic Au(III) complex exhibited four additional bands 980 nm (10204 cm^{-1}), 442 nm (22624 cm^{-1}), 362 nm (27624 cm^{-1}) and 242 nm (41322 cm^{-1}) attributed to the transitions $^1A_1g \rightarrow {}^1B_1g_{(\upsilon 1)}$, $^1A_1g \rightarrow {}^1A_2g_{(\upsilon 2)}$, $^1A_1g \rightarrow {}^1Eg_{(\upsilon 3)}$ and intra ligand, respectively of square planar geometry (hybridization dsp^2) (Al-Saif and Refat 2012).

Table 5
Electronic spectra (in nm), magnetic moment, geometry and hybridization of metal complexes.

Compounds	Absorption Bands (nm)	Transitions	μ_{eff} (B.M)	Geometry	Hybridization
6-MBTAMB	434	n →π*	-	-	-
	312	π →π*			
	242	π →π*			
Ag(I)-Complex	446	dπ(Ag)$^{+1}$→ π*(L)(C.T)	Dia	Tetrahedral	sp^3 (Low spin)
	362	Intra ligand			
	326	Intra ligand			
	240	Intra ligand			
Pt(IV)-Complex	486	$^1A_1g \rightarrow {}^1T_1g_{(F)}(\upsilon_1)$	Dia	Octahedral (Regular)	d^2sp^3 (Low spin)
	380	$^1A_1g \rightarrow {}^1T_2g_{(F)}(\upsilon_2)$			
	264	$^1A_1g \rightarrow {}^1T_1g_{(p)}(\upsilon_3)$			
Au(III)-Complex	980	$^1A_1g \rightarrow {}^1B_1g(\upsilon_1)$	Dia	Square Planer	dsp^2 (Low spin)
	442	$^1A_1g \rightarrow {}^1A_2g(\upsilon_2)$			
	362	$^1A_1g \rightarrow {}^1Eg(\upsilon_3)$			
	242	Intra ligand			

B.M = Bohr Magneton.

Based on the previously described chemical and spectral analyses, it may be possible to suggest the structural formula of chelate complexes as illustrated in Figure 9.

3.9. X-ray diffraction study (XRD)

X-ray diffraction provides direct information about the molecular or atomic arrangement in solid-state materials (El-Boraey and El-Domiaty 2021; Begum, Hussain, and Rahman 2012). The X-ray diffractograms were determined for ligand (6-MBTAMB), $[Ag(L)H_2O].H_2O$, $[Pt(L)Cl_3].H_2O$ and $[Au(L)Cl]Cl.H_2O$, respectively. The intensity of diffracted *CuKα* radiation was calculated in 2Θ between (0° to 80°), λ = 1.54060 Å and the generator settings (30 mA/40 kV). The Xpert High Score computer program measures parameters of diffraction spectra using peaks identified by diffraction peaks (Cardona et al. 2017). The results showed their semi crystalline nature (Figure 10).

Using Bragg's equation (Al-Hussainawy and Kyhoiesh 2019), major refluxes were calculated and corresponding d-spacing values were measured; $n\lambda = 2d\sin\theta$, where (d) is the spacing between the crystalline levels, (n) is an integer (1,2,3 ..), (λ) is the wavelength of X-ray CuKα = 1.540598 A°, (Θ) is the diffraction angle. The patterns of the ligand (6-MBTAMB), Ag(I), Pt(IV) and Au(III) complexes show many peaks with maximum intensities at 2Θ = 15.6408, 16.1045, 15.6597 and 15.5974 which correspond to d-spacing (5.66581, 5.04920, 5.65901 and 5.68148 A°), respectively.

The Debye-Scherrer equation (Mustapha et al. 2019) was used to determine the average crystallite size of the particles and their size distributions; $D = k\lambda / \beta\cos\theta$, where (D) is the average diameter of the crystallite, (k) is the shape factor (0.891), (λ) is the X-ray wavelength (0.15405 nm), (Θ) is the diffraction angle, and (β) is line broadening at half the maximum intensity (FWHM) in radian of a reported peak. Experimental average sizes were 27.51 nm for 6-MBTAMB, 36.73 nm for Ag(I), 38.52 nm for Pt(IV), and 42.96 nm for Au(III). Compounds are shown to have nanostructure properties based on their crystallite size (Serafińczuk et al. 2020). The crystallographic parameters for (6-MBTAMB) and chelate complexes are shown in Table 6.

Table 6
Crystallographic data and structure refinement details for (6-MBTAMB) and chelate complexes.

Characteristic	6-MBTAMB	Ag(I)-Complex	Pt(IV)-Complex	Au(III)-Complex
Chemical Formula:	$C_{17}H_{15}N_3O_3S$	$C_{17}H_{18}N_3O_5SAg$	$C_{17}H_{16}N_3O_4SCl_3Pt$	$C_{17}H_{16}N_3O_4SCl_2Au$
Formula weight:	341.38	484.27	659.83	626.26
Crystal system:	Cubic	Tetragonal	Monoclinic	Monoclinic
Space group:	Fd3m	P4/nmm	$P2_1/c$	P12/m1
Space group number:	227	129	14	10
a (A°):	23.2500	4.5050	8.4050	6.6380
b (A°):	23.2500	4.5050	10.1830	6.8260
c (A°):	23.2500	10.2300	13.7310	16.3690
Alpha (°):	90.0000	90.0000	90.0000	90.0000
Beta (°):	90.0000	90.0000	97.2400	92.1500
Gamma(°):	90.0000	90.0000	90.0000	90.0000
Calculated density(g/cm^3):	-	9.53	1.81	1.04
Measured density (g/cm^3):	-	-	-	-
Volume of cell (10^6pm^3):	12568.08	207.62	1165.84	741.17
Z:	8.00	2.00	4.00	2.00
RIR:	-	-	-	-
Start Position [°2Th.]	9.9250	3.0000	9.9250	9.9250
End Position [°2Th.]	80.0750	80.0750	80.0750	80.0750
Step Size [°2Th.]	0.0500	0.0600	0.0500	0.0500
Scan Step Time [s]	1.0000	1.0000	1.0000	1.0000
Scan Type	Continuous	Continuous	Continuous	Continuous
Offset [°2Th.]	0.0000	0.0000	0.0000	0.0000
Divergence Slit Type	Fixed	Fixed	Fixed	Fixed
Divergence Slit Size [°]	1.0000	1.0000	1.0000	1.0000
Specimen Length [mm]	10.00	10.00	10.00	10.00
Receiving Slit Size [mm]	0.1000	0.1000	0.1000	0.1000
Measurement Temperature [°C]	25.00	25.00	25.00	25.00
Anode Material	Cu	Cu	Cu	Cu
K-Alpha1[A°]	1.54060	1.54060	1.54060	1.54060
K-Alpha2 [A°]	1.54443	1.54443	1.54443	1.54443
K-Beta [A°]	1.39225	1.39225	1.39225	1.39225
K-A2 / K-A1 Ratio	0.50000	0.50000	0.50000	0.50000
Generator Settings	30 mA, 40 kV	30 mA, 40 kV	30 mA, 40 kV	30 mA, 40 kV
Diffractometer Type	Undefined	Undefined	Undefined	Undefined
Diffractometer Number	1	1	1	1
Goniometer Radius [mm]	240.00	240.00	240.00	240.00
Dist. Focus-Diverg. Slit [mm]	91.00	91.00	91.00	91.00
Incident Beam Monochromator	No	No	No	No
Spinning	No	No	No	No
Reference code:	00-043-0316	00-037-1301	00-031-1996	00-029-1773

3.10. Thermogravimetry Analysis

The thermal stabilities of ligand and its metal complexes were investigated by thermogravimetric analysis (TGA-DTA), under N_2 atmosphere at a heating rate of 10°C min^{-1} in the temperature range RT to 900°C using Pt crucible (Figure 11). The nature of the proposed chemical change with temperature and the percent of metal oxide obtained (Bowman and Rogers 1966; Turan et al. 2021; Ammar et al. 2018; Al-Maydama et al. 2006; Sabir, Malik b, and Iftikhar 1994) are given in Table 7.

The TGA curve of the ligand (6-MBTAMB) shows three steps of weight loss within the temperature range of 31.70-837.95°C. The first step at 31.70-299.92ºC (Cal./Found% 61.58/61.79) associated with DTA peaks at 69.77, 99.97°C that is assigned to the release of ($C_{10}H_{14}N_2O_3$). The second step at 299.92-470.96 ºC (Cal./Found% 14.95/15.51) corresponds to the loss of (C_3HN). The third step at 470.96-837.95 ºC (Cal./Found% 7.97/7.71) due to loss of ($C_2S_{0.1}$), residual carbon atoms.

The thermogram of the Ag(I)-Complex gives a decomposition pattern of two steps within the temperature range of 38.07-837.59°C. The first decomposition within the temperature range of 38.07-200.53°C (Cal./Found% 15.29/15.47) corresponds to the loss of ($C_3H_6O_2$). The second decomposition within the temperature range of 200.53-837.59 ºC (Cal./Found% 35.55/35.65) corresponds to the loss of ($C_{10}H_8N_2O$). The DTA curve begins at 127.25°C (endothermic) and ends at 197.82, 224.75, and 313.10°C, which are exothermic peaks.

The thermal degradation of the Pt(IV)-Complex shows two decomposition steps at the temperature range of 25.85–838.24°C. The first step occurs within the temperature range 25.85-296.49°C (Cal./Found% 53.13/53.06) corresponds to the loss of ($C_{13}H_{14}N_3O_2Cl_3$). The second step corresponds to the removal of the ($C_4H_2SPt_{0.29}$) molecule with mass loss of (Cal./Found% 21.01/21.16). These steps are accompanied by endothermic peaks at 128.95, 230.16°C, respectively.

On the other hand, the TGA curve of the Au(III)-Complex shows two steps of decomposition during thermal degradation within the temperature range of 28.04–823.17°C. The first decomposition step occurs in the range 28.04-299.90°C (Cal./Found% 70.98/70.92) and corresponds to the loss of ($C_{17}H_{16}N_3O_2SCl_2Au_{0.24}$) molecule. The final decomposition step occurs in the temperature range 299.50-823.17 ºC (Cal./Found% 28.98/29.06) and corresponds to the loss of ($Au_{0.76}O_2$). The DTA curve shows two endothermic peaks were observed first 128.95°C, second 230.16°C.

However, the TGA curves beyond 900°C have been observed in all the complexes indicating further weight loss, implying that a metal oxide may be the final product.

Table 7
Thermal analysis data of the (6-MBTAMB) and metal complexes.

Compound	Decomposition	TG Range (°C)	Mass loss%	Total mass Loss %	DTA(°C)				Evolved moieties
T_i	T_f	T_{max}	Nature of peaks	Found (Calculated)					
6-MBTAMB	1st Step	31.70-299.92	61.79(61.58)	83.99	81.96	91.35	69.77	Endothermic (+)	Loss of $[C_{10}H_{14}N_2O_3]$
$C_{17}H_{15}N_3O_3S$	2nd Step	299.92-470.96	15.51(14.95)		110.21	116.47	99.97	Endothermic (+)	Loss of $[C_3HN]$
341.38	3rd Step	470.96-837.95	7.71(7.97)						Loss of $[C_2S_{0.1}]$
	Residue	>837.95	16.01(15.48)						Loss of a part of the ligand
Ag(I)-Complex	1st Step	38.07-200.53	15.47(15.29)	50.58	120.78	135.04	127.25	Endothermic (+)	Loss of $[C_3H_6O_2]$
$[Ag(L)(H_2O)].H_2O$	2nd Step	200.53-837.59	35.65(35.55)		165.66	208.47	197.82	Exothermic (-)	Loss of $[C_{10}H_8N_2O]$
$C_{17}H_{18}AgN_3O_5S$	Residue	>837.59	49.42(49.14)		208.46	274.35	224.75	Exothermic (-)	Loss of a part of the ligand
484.27					289.08	341.39	313.10	Exothermic (-)	
Pt(IV)-Complex	1st Step	25.85-296.49	53.06(53.13)	74.15	118.36	160.71	128.95	Endothermic (+)	Loss of $[C_{13}H_{14}N_3O_2Cl_3]$
$[Pt(L)Cl_3].H_2O$	2nd Step	296.49-838.24	21.16(21.01)		167.24	286.76	230.16	Endothermic (+)	Loss of $[C_4H_2SPt_{0.29}]$
$C_{17}H_{16}PtN_3O_4SCl_3$	Residue	>838.24	25.85(25.84)						Loss of a part of the ligand
659.83									
Au(III)-Complex	1st Step	28.04-299.80	70.92(70.98)	99.98	109.23	148.33	120.71	Endothermic (+)	Loss of $[C_{17}H_{16}N_3O_2SCl_2Au_{0.24}]$
$[Au(L)Cl]Cl.H_2O$	2nd Step	299.80-823.17	29.06(28.98)		214.26	272.22	235.17	Endothermic (+)	Loss of $[Au_{0.759}O_2]$
									Loss of a part of the ligand
$C_{17}H_{16}AuN_3O_4SCl_2$	Residue	>823.17	0.02(0.03)						
626.26									

T_i = Initial temperature, T_f = Final temperature.

3.11. FE-SEM Analysis

Field emission scanning electron microscopy (FE-SEM) of the ligand (6-MBTAMB) and metal complexes studies the surface morphology and shape of the particles and aggregation, in addition to the distribution of these particles. The field emission scanning electron microscope technique was employed at a cross-sectional distance of (200 nm) and a magnification force of (Mag = 20.00 KX). FE-SEM images of the 6-MBTAMB and its complexes can be seen in Figure 12. Using the Image J software, particle sizes were calculated (Tyuftin et al. 2021). The (FESEM) image of the ligand (6-MBTAMB) analysis is shown as spherical crystals with an average particle size of 90.54 nm and a ratio of less than totality. Furthermore, FE-SEM of the Ag(I)-Complex revealed the particles to be spherical with an average size of 87.67 nm. Pt(IV)-Complex and Au(III)-Complex micrographs were faceted with granular and spherical particles of different sizes of 80.08 and 40.57 nm, respectively. The FE-SEM micrographs of 6-MBTAMB and its chelates complexes vary considerably because metal ions coordinate to donor sites (Baraka, Hall, and Heslop 2007). Show that the grains of the prepared compounds are smaller than (100) nm, It is within the nanoscale range. Where the surface area increases effectively and thus enters the (Quantitative effect) to create new energy levels that move the electron more free. Characteristics of the ligand and its complexes enabled us to study in medicine and the susceptibility of these compounds to the inhibition of many types of cancers (Al-adilee and Hessoon 2019). Various conditions have been used to synthesize nanoparticles of different sizes and shapes e.g. irregular multilateral shapes (1.5-2 μm), aggregate particles (600-700 nm), isolated particle (100-150 nm), porous structure (40 nm), and nanoparticles (28-32 nm) (Amschler et al. 2014).

3.12. Antimicrobial activity of azo dye ligand (6-MBTAMB) and all complexes

The antimicrobial activity of ligands (6-MBTAMB) and their metal complexes Ag(I), Pt(IV) and Au(III) have been studied by diffusion method against microorganisms representing Gram-positive bacteria *(Staphylococcus aureus*), Gram-negative bacteria (*Escherichia coli*) and antifungal (*Aspergillus niger*) at the concentration 0.2 mg/ml presented in Table 8 and Figure 13. Antibiotics (Novobiocin) and (Cycloheximide*)* have traditionally been used. A study has shown that ligand and some transition metal complexes exert good antimicrobial activity against bacteria and fungi tested. Thus, benzothiazole moiety compounds may have an advantage since they target more severe clinical conditions than bacteriostatic agents (Egorova et al. 2021). The antibacterial activity from the result obtained clearly that the Ag(I)-Complex has exhibited good activity against both bacteria (Gram-negative & Gram-positive) as compared to ligand (6-MBTAMB) and standard drug (Novobiocin). The antifungal activity result revealed that the ligand (6-MBTAMB) show highly active as compared to metal complexes and standard antifungal drugs (Cycloheximide). In an inhibition zone test with DMSO, there were no inhibition zones. A comparative study of values indicated that the metal complexes exhibited promising antimicrobial activity as compared to free ligand, the enhanced activity of the complexes can be rationalized based on Tweedy's chelation theory (Mishra et al. 2021). The chelation theory suggests that this makes sense. Chelation reduces the polarity of the metal ion, primarily due to its partial sharing of its positive charge with the donor groups and delocalization of π-electron on the whole chelate ring. A chelate can reduce not only the polarity of the metal ion, but it can also increase the lipophilic character of the chelate, facilitating the interaction between the metal ion and the lipid. Cellular processes may be interfered with due to the breakdown of the permeability barrier. Geometry and charge distribution around the molecule must match those around the pores of the bacterial cell wall to prevent penetration through the wall by the toxic agent and the toxic reaction within the pores. Therefore, carboxylate, methyl, and methoxy substituents on the benzothiazole moiety and the phenyl ring impart good antibacterial activity. However, the activity has always been greater for the metal complexes than the free ligands (Pitchumani Violet Mary, Shankar, and Vijayakumar 2019; Ekennia et al. 2017; Pramanik et al. 2015; Joshi and Kumar 2014).

Table 8
Antimicrobial activity data of ligand (6-MBTAMB) and its complexes (inhibition zone mm).

Compound	Bacteria		Fungi
	Gram-Positive	Gram-Negative	
	Staphylococcus aureus	Escherichia coli	Aspergillus Niger
6-MBTAMB	+++	+	+++
Ag(I)-Complex	+++	+++	+++
Pt(IV)-Complex	+++	++	+
Au(III)-Complex	+++	++	-
Novobiocin	+	-	□□□□□□□□
Cycloheximide	□□□□□□□□	□□□□□□□□	-
DMSO	-	-	-
Highly active = + + + (inhibition zone > 20 mm)			

Moderately active = + + (inhibition zone 15-20 mm)

Weakly active = + (inhibition zone 10-15 mm)

Inactive = - (inhibition zone < 10 mm

3.13. Molecular docking studies

In silico molecular docking was conducted to further assess the anticancer activities of these compounds. The molecular docking study of synthesized compounds was used to examine biomolecular interactions of new compounds, which supports the design and reconstruction of drugs as effective inhibitors for the development of diseases (Manju, Kishore, and Kumar 2011). Molecular docking was performed further on compounds to interpret theirs in vitro activities against FGF Receptor 2 (FGFR2) kinase domain harboring the pathogenic gain of function K659E mutation identified in endometrial cancer based on their ligand-protein interactions (Chen et al. 2013; Bian and Xie 2018). Molecular docking analyses (PDB ID: 4J97) have been conducted to predict the affinity and preferred orientation of each docking pose. Results of the docking study are expressed in terms of enzyme binding free energy (ΔG). Figures 14, 15 and 16 displayed the intermolecular interactions of FGFR2 inhibitors with the active site of amino acid residues from the best docking pose in 3D and 2D predictions. Based on the binding energy of FGFR2 inhibitors, the penetration through protein holes of compounds is shown in Tables 9 and 10. Various intermolecular interactions with amino acid residues determined the binding affinity of ligands. The ligand (6-MBTAMB) were able to reveal diverse noteworthy interactions with the active site amino acids (Ala 567, Asp 644). The Ag(I)-Complex exhibits two H-bond interactions represented (Figure 15b) with the active site amino acids (Val 495, Asp 644). Moreover, Pt(IV)-Complex also exhibits seven H-bond with residues of (Gly 490, Ala 491, Gly 493, Lys 517, Arg 630, Asn 631). In another hand, Au(III)-Complex has interactions with active site amino acids (Leu 487, Val 495, Ala 567 and Asn 571), respectively. Compounds like these interact strongly with residues that tightly bind to complexes, which prevent their functions from being carried out by the ligand, which stops the metabolism of cancerous cells (Varghese et al. 2021). Molecular docking is a tool used in modern drug design to analyze how drugs interact with their receptors (Abdolmaleki, B Ghasemi, and Ghasemi 2017). Normal cells contain FGFR, which is involved in embryogenesis, tissue homeostasis, tissue repair, wound healing, and inflammation. As a result, inhibiting the FGFR signalling pathway presents a promising therapeutic option for cancer (Chaudhary and Mishra

2016; Liu et al. 2020). According to Do-Hee et al. (Kim et al. 2016), FGFR2 would serve as an efficient target for inhibiting the migration and/or invasion of endometrial cancer cells harboring FGFR2-activating mutations. Taken together, this is undoubted that AP24534 possesses excellent inhibitory ability against FGFR2-deregulated endometrial cancer cells. In addition, the antitumor effect of AP24534 against endometrial cancer cells with activating FGFR2 mutations might be mainly associated with the blockade of ERK, PLCg and STAT5 signal transduction.

Table 9
Binding energy values of FGFR2 protein.

Compound	S (Kcal/mol)	RMSD_refine	E.conf	E. place	E. score1	E. refine	E. score2
6-MBTAMB	-6.4561	0.7306	3.0706	-96.5378	-10.0700	-26.9137	-6.4561
Ag(I)-Complex	-6.8556	2.3956	-258.6523	-67.9934	-10.2981	-47.0924	-6.8556
Pt(IV)-Complex	-5.8246	1.4380	-150.4951	-66.9427	-11.4781	-25.9739	-5.8246
Au(III)-Complex	-6.0690	1.0906	-7.5073	-78.8561	-9.7973	-30.7756	-6.0690

S = the final score is the score of the last step, RMSD_refine = the mean square deviation between the laying before refinement and after refinement pose, E_conf = energy conformer, E_place = score of the placement phase, E_scor1 = score the first step of notation, E_refine = score refinement step and number of conformations generated by ligand E_scor2 = score the first step notation, number of poses = Number of conformations.

Table 10
The binding residues of receptors in the binding site for compounds.

Compound	Active site residues	Interactions
6-MBTAMB	Ala 567	Greasy (backbone donor) …..O
	Asp 644	Acidic (side chain donor) ……S
Ag(I)-Complex	Val 495	Greasy (backbone donor) benzene ring
	Asp 644	Acidic (side chain donor) ……H_2O
Pt(IV)-Complex	Gly 490	Polar (side chain accepter) ……Cl
	Ala 491	Greasy (backbone donor) ……Cl
	Gly 493	Polar (side chain accepter) ……O
	Lys 517	Basic (backbone accepter) …..O
		Basic (backbone accepter) …..Cl
	Arg 630	Basic (backbone accepter) ……S
	Asn 631	Polar (side chain accepter) ……S
Au(III)-Complex	Leu 487	Greasy (backbone donor) thiazole ring…H
	Val 495	Greasy (backbone donor) benzene ring…H
	Ala 567	Greasy (backbone donor) …..S
	Asn 571	Polar (side chain accepter) …..Cl

3.14. DPPH Scavenging Activity

DPPH (1,1-diphenyl-2-picrylhydrazyl) becomes a free radical by the spare electron delocalizing over the whole molecule, which means that the molecule does not dimerize, unlike most other free radicals (Purushotham et al. 2019). Hydrogen donors serve as antioxidants, this method identifies compounds that act as radical scavengers. The DPPH• can accept hydrogen from an anti-oxidant. A DPPH• radical is one of the few stable and commercially available organic nitrogen radicals. The antioxidant effect in a test sample is proportional to the disappearance of DPPH• (Parisi et al. 2016). Using ascorbic acid as a standard, all synthesized compounds were evaluated for their free radical scavenging activity. For each compound and ascorbic acid, IC_{50} values were calculated and summarized in Table 11 and shown in Figures 18, 19. Based on the low IC_{50} values, it is evident Ag(I) metal complex has the highest antioxidant activity in this DPPH assay. IC_{50} values at higher concentrations were noted for the remaining compounds with medium to lower activity. This study determined the mechanism of free radical scavenging activity shown in Figure 17 (Kyhoiesh and Al-Adilee 2021).

Table 11
Antioxidant activity from the analysis in vitro for ligand (6-MBTAMB) and its metal complexes.

DPPH Radical Scavenging Activity %										
Concentration (µg/ml)	Ascorbic Acid		6-MBTAMB		Ag(I)-complex		Pt(IV)-complex		Au(III)-complex	
	Mean ± SD		Mean ± SD		Mean ± SD		Mean ± SD		Mean ± SD	
12.5	80.290456	1.0373443	26.661985	2.9346315	32.412523	1.6921063	29.579472	0.9347738	32.634032	2.840859
25	85.580912	1.8758445	37.617041	1.2331055	40.906998	2.0420668	35.257780	0.61451732	42.494172	1.199730
50	92.773167	5.4500907	49.953183	0.8494965	71.500920	0.7700611	46.923259	3.29902686	64.522144	1.088605
100	99.031811	0.3169139	64.700374	1.2047855	86.901473	0.7254121	59.158945	1.35985631	85.011655	0.944271
200	99.446749	0.0598911	74.227528	2.3679375	88.236648	1.9743813	79.472558	0.37715628	93.263403	0.397639
400	99.515905	0.0598911	85.065543	1.9816979	93.162983	0.0690607	89.159657	1.23453371	93.682983	0.664642
R^2	0.9950		0.9964		0.9836		0.9813		0.9905	
IC_{50}	3.152		47.79		26.76		49.62		27.82	

3.15. Anticancer effect

Cell lines from cancerous tissues can be used to study human cancer both in vitro and in vivo. According to statistics, endometrial cancer is the fourth most common kind of cancer in women (Ying et al. 2021). There are two subtypes of endometrial cancer. Type I (endometrioid histology) and type II (serous or clear cell histology) exhibit vastly different clinical and pathologic features (Liu, Enriquez, and Ford 2021; Johnatty et al. 2021). Using a cell viability assay, the cytotoxic activity of the ligand (6-MBTAMB) and Au(III)-Complex against endometrial cancer cells (MFE-296) and the effect of normal cells human umbilical vein endothelial cell (HUVEC) at different concentrations (25, 50, 100, 200, and 400 µg/mL) were studied (MTT assay). The ligand (6-MBTAMB) inhibited tumor cell death at a concentration of 400 µg/ml, with a cytotoxic efficacy of (89.12%). On the other hand, the Au(III)-complex inhibited (MFE-296) to (97.40%) at a concentration of 400 µg/mL, whereas the normal cellular cell (HUVEC) had no effect at the same concentration. Similarly, all compounds tested were inhibited the most when concentrations of (400 µg/ml) were incubated for 24 hours, while concentrations of (25 µg/ml) inhibited the least. The selectivity index (SI), which indicates cytotoxicity of the compound against cancer cells while it is relatively safe against normal cells, was calculated by comparing the IC_{50} values for each cell line. Au(III)-complex showed selective cytotoxicity against cancer cell lines with IC_{50} = 43.44 µg/ml, but was very healthy against normal cells with IC_{50} = 148.20 µg/ml. Tables 12 and 13 give the viability rate values for selected compounds after 24 hours of treatment with various concentrations of MFE-296 and HUVEC cells and calculate the 50% inhibitory concentration.

Table 12
Evaluation of cytotoxicity of (6-MBTAMB) against MFE-296 cancer cell line after incubation (24 hours) at (37°C) and HUVEC cell line.

Concentration (µg/mL)	6-MBTAMB					
	Cancer line cells			Normal line cells		
	MFE-296			HUVEC		
Cell Viability		% Cell Inhibition	Cell Viability		% Cell Inhibition	
Mean	SD		Mean	SD		
0	100.0000821		1.916969709	100.0049425		1.606326455
25	86.82381317	4.084800092	13.17618683	87.60739734	1.286090448	12.39260266
50	76.64401662	3.47428312	23.35598338	74.79797356	3.343074078	25.20202644
100	48.1570053	3.737808647	51.8429947	63.7184398	2.639560109	36.2815602
200	27.46903166	5.098662992	72.53096834	46.70785452	2.780409215	53.29214548
400	10.87733299	0.924348782	89.12267653	39.83039866	1.464293909	60.16961087
IC_{50}	100.4			189.6		

Table 13

Evaluation of cytotoxicity of Au(III)-Complex against MFE-296 cancer cell line after incubation (24 hours) at (37°C) and HUVEC cell line.

Concentration (µg/mL)	Au(III)-Complex					
	Cancer line cells			Normal line cells		
	MFE-296			HUVEC		
Cell Viability		% Cell Inhibition	Cell Viability		% Cell Inhibition	
Mean	SD		Mean	SD		
0	100.0000821		1.916969709	100.0049425		1.606326455
25	74.42744802	1.513202834	25.57255198	86.45413732	1.388831113	13.54586268
50	44.75005726	2.300495488	55.24994274	67.96078916	1.858937204	32.03921084
100	26.11446196	4.212728393	73.88553804	54.98661395	2.374650571	45.01338605
200	13.80019194	2.155290431	86.19980806	45.73170229	2.705228629	54.26829771
400	2.594206218	1.913010387	97.40579378	34.84575147	1.871216556	65.15424853
IC_{50}	43.44			148.2		

4. Conclusion

Newly synthesized Ag(I), Pt(IV) and Au(III) metal complexes based on benzothiazole azo dye ligand have been prepared and underwent structural identification applying analytical (elements content, thermogravimetric analysis) and spectroscopic (^{1}H NMR, ^{13}C NMR, IR, mass and UV–Vis spectra) tools as well as magnetic susceptibility measurements. Elemental and spectroscopic results confirmed 1:1 (M:L) stoichiometry of metal complexes. The molar conductance measurements proved the presence of the chloride ion outside the coordination sphere in the Au(III) complex, giving the 1:1 electrolyte nature but non-electrolyte in the rest of the metal complexes. The applied tools combined have confirmed the metal complexes to be formulated as $[Ag(L)(H_2O)].H_2O$, $[Pt(L)Cl_3].H_2O$, $[Au(L)Cl]Cl.H_2O$. Crystallinity, parameters, and morphology of the sample were assessed with X-ray diffraction (XRD) and field emission scanning electron microscope (FESEM). These investigations have shown that the tridentate ligand is coordinated to the metal ions via the N atom of the azomethine group, the N atom of the azo group and the O atom of the carboxylate group as donor atoms. The microbial activates of the organic ligand with metal complexes were screened in vitro against various bacteria and fungi. The results showed that the ligand and metal complexes have generally higher activity than standard antibacterial (Novobiocin) and antifungal (Cycloheximide). In molecular docking, the binding affinity and interaction of the synthesized ligand and its metal complexes are tight with the binding sites of FGF Receptor 2 (FGFR2) proteins, which contributes to designing the potent chemotherapy agent. DPPH radical scavenging assays are used to evaluate the antioxidant activity of the ligand and its complexes. By comparing the antioxidant activity of produced new azo compounds with a known antioxidant, such as ascorbic acid, their antioxidant activity was determined. In the cytotoxicity assays conducted on 6-MBTAMB and Au(III) metal complex using endometrial cancer cell line MFE-296, and compared with HUVEC, the anticancer efficiency assayed the viability of the cells, it can be concluded that ligand and Au(III) metal complex possess good cytotoxic property and selectivity against endometrial cancer cell line (MFE-296) cells.

Declarations

Acknowledgements

Acknowledgements and thanks to Prof. Khalid Al-Adilee, for his encouragement and moral support during the scientific research.

Compliance with ethical standards

Conflict of interest The authors declare that they have no conflict of interest.

References

1. Abdolmaleki A, Ghasemi B, Ghasemi J F (2017) Computer aided drug design for multi-target drug design: SAR/QSAR, molecular docking and pharmacophore methods. Curr Drug Targets 18(5):556–575
2. Ahmed I, Atta AH, Refat MS (2014) Complexation of gadolinium (III) and terbium (III) with nalidixicacid (NDX): Molar conductivity, thermal and spectral investigation. Int J Electrochem Sci 9:5187–5203
3. Al-Adilee J, Jaber A (2018) Synthesis, Characterization and Biological Activities of Some Metal Complexes Derived from Azo Dye Ligand 2-[2'-(5-Methyl thiazolyl) azo]-5-dimethylamino Benzoic Acid. Asian J Chem 30(7):0000–0000
4. Al-Adilee K, Kyhoiesh HA (2017) Preparation and identification of some metal complexes with new heterocyclic azo dye ligand 2-[2–-(1-Hydroxy-4-Chloro phenyl) azo]-imidazole and their spectral and thermal studies. J Mol Struct 1137:160–178
5. AL-Adilee KJ, Abass AK, Taher AM (2016) Synthesis of some transition metal complexes with new heterocyclic thiazolyl azo dye and their uses as sensitizers in photo reactions. J Mol Struct 1108:378–397

6. Al-Adilee KJ, Abedalrazaq KA, Al-Hamdiny ZM (2013) Synthesis and spectroscopic properties of some transition metal complexes with new azo-dyes derived from thiazole and imidazole. Asian J Chem 25(18):10475
7. Al-Adilee KJ, Hesson H (2015) Synthesis, identification, structural, studies and biological activity of some transition metal complexes with novel heterocyclic azo-Schiff base ligand derived from benzimidazole. J Chem Pharm Res 7(8):89–103
8. Al-adilee KJ, Hessoon H, Synthesis (2019) Spectral Properties And Anticancer Studies of Novel Hetrocyclic Azo Dye Ligand Derived From 2-Amino-5-methyl thiazole with Some Transition Metal Complexes. In: Journal of Physics: Conference Series, vol 1. IOP Publishing, p 012094
9. Al-Adilee KJ, Waheeb AS (2020) Preparation, spectroscopic and anticancer studies of metal antibiotic Chelation Ni (II), Cu (II) and Zn (II) 4, 5-dimethyl Thiazolylazo complexes. In: Journal of Physics: Conference Series, vol 1. IOP Publishing, p 012057
10. Al-Hussainawy M, Kyhoiesh H (2019) Synthesis, Spectral Characterization and Biological Activity of 2-[2□-(1-Amino-1, 5-Dinitrophenyl) azo]-Imidazole. Journal of Global Pharma Technology 11(7):165–174
11. Al-Maydama H, El-Shekeil A, Khalid MA, Al-Karbouly A (2006) Thermal degradation behaviour of some polydithiooxamide metal complexes. Eclet Quim 31:45–52
12. Al-Saif FA (2014) Spectroscopic elucidation, conductivity and activation Thermodynamic parameters studies on Pt (IV), Au (III) and Pd (II) 1, 5-dimethyl-2-phenyl-4-[(thiophen-2-ylmethylene)-amino]-1, 2-dihydro-pyrazol-3-one Schiff base complexes. Int J Electro chem Sci 9:398–417
13. Al-Saif FA, Refat MS (2012) Ten metal complexes of vitamin B3/niacin: Spectroscopic, thermal, antibacterial, antifungal, cytotoxicity and antitumor studies of Mn (II), Fe (III), Co (II), Ni (II), Cu (II), Zn (II), Pd (II), Cd (II), Pt (IV) and Au (III) complexes. J Mol Struct 1021:40–52
14. Ammar RA, Alturiqi AS, Alaghaz A-NM, Zayed ME (2018) Synthesis, spectral characterization, quantum chemical calculations, in-vitro antimicrobial and DNA activity studies of 2-(2'-mercaptophenyl) benzothiazole complexes. J Mol Struct 1168:250–263
15. Amschler K, Erpenbeck L, Kruss S, Schön MP (2014) Nanoscale integrin ligand patterns determine melanoma cell behavior. ACS Nano 8(9):9113–9125
16. Araki T, Muramatsu Y, Tanaka K, Matsubara M, Imai Y (2001) Riluzole (2-amino-6-trifluoromethoxy benzothiazole) attenuates MPTP (1-methyl-4-phenyl-1, 2, 3, 6-tetrahydropyridine) neurotoxicity in mice. Neurosci Lett 312(1):50–54
17. Bain GA, Berry JF (2008) Diamagnetic corrections and Pascal's constants. J Chem Educ 85(4):532
18. Bank-tiedosto PD, Berman HM, Westbrook J, Feng Z, Gilliland G, Bhat TN, Weissig H, Shindyalov (2000) IN ja Bourne, PE, The Protein Data Bank Nucleic Acids Res 28:235-242
19. Baraka A, Hall P, Heslop M (2007) Preparation and characterization of melamine–formaldehyde–DTPA chelating resin and its use as an adsorbent for heavy metals removal from wastewater. Reactive and Functional Polymers 67(7):585–600
20. Begum A, Hussain A, Rahman A (2012) Effect of deposition temperature on the structural and optical properties of chemically prepared nanocrystalline lead selenide thin films. Beilstein J Nanotechnol 3(1):438–443
21. Berger C, Dawson LR (1952) Determination of Chloride Ion in Formamide Solutions. Anal Chem 24(6):994–996
22. Bhat M, Belagali S (2014) Synthesis of Azo-Bridged Benzothiazole-Phenyl Ester Derivatives via Steglich Esterification. Int J Curr Eng Techol 4(4):2711–2715
23. Bian Y, Xie X-QS (2018) Computational fragment-based drug design: current trends, strategies, and applications. AAPS J 20(3):59
24. Boulikas T, Vougiouka M (2003) Cisplatin and platinum drugs at the molecular level. Oncol Rep 10(6):1663–1682
25. Bowman P, Rogers L (1966) Effect of metal ion and ligand on thermal stability of metal amine complexes. J Inorg Nucl Chem 28(10):2215–2224
26. Cardona DMM, Wongsa-Ngam J, Jimenez H, Langdon TG (2017) Effects on hardness and microstructure of AISI 1020 low-carbon steel processed by high-pressure torsion. Journal of Materials Research and Technology 6(4):355–360
27. Chandra S, Gupta LK (2005) Electronic, EPR, magnetic and mass spectral studies of mono and homo-binuclear Co (II) and Cu (II) complexes with a novel macrocyclic ligand. Spectrochim Acta Part A Mol Biomol Spectrosc 62(4–5):1102–1106
28. Chaudhary KK, Mishra N (2016) A review on molecular docking: novel tool for drug discovery. databases 3 (4):1029
29. Chen H, Huang Z, Dutta K, Blais S, Neubert TA, Li X, Cowburn D, Traaseth NJ, Mohammadi M (2013) Cracking the molecular origin of intrinsic tyrosine kinase activity through analysis of pathogenic gain-of-function mutations. Cell reports 4(2):376–384
30. Chiu C-T, Lai C-H, Huang Y-H, Yang C-H, Lin J-N (2021) Comparative analysis of gradient diffusion and disk diffusion with agar dilution for susceptibility testing of Elizabethkingia anophelis. Antibiotics 10(4):450
31. Choueiry F, Singh S, Sircar A, Laliotis G, Sun X, Chavdoula E, Zhang S, Helmig-Mason J, Hart A, Epperla N (2021) Integration of Metabolomics and Gene Expression Profiling Elucidates IL4I1 as Modulator of Ibrutinib Resistance in ABC-Diffuse Large B Cell Lymphoma. Cancers 13(9):2146
32. Christensson N, Zidek K, Magdaong NCM, LaFountain AM, Frank HA, Zigmantas D (2013) Origin of the bathochromic shift of astaxanthin in lobster protein: 2D electronic spectroscopy investigation of β-crustacyanin. J Phys Chem B 117(38):11209–11219
33. Chu Q, Medvetz DA, Pang Y (2007) A polymeric colorimetric sensor with excited-state intramolecular proton transfer for anionic species. Chem Mater 19(26):6421–6429
34. Currie L (2018) Synthesis and properties of gold (III) pincer complexes with sulfur ligands. University of East Anglia
35. D'ulivo A, Lampugnani L, Zamboni R (1991) Interference of copper, silver and gold in the determination of selenium by hydride generation atomic fluorescence spectrometry: an approach to the studies of transition metal interferences. J Anal At Spectrom 6(7):565–571
36. da Silva Maia PI, Deflon VM, Abram U (2014) Gold (III) complexes in medicinal chemistry. Future medicinal chemistry 6(13):1515–1536
37. Dadmal TL, Katre SD, Mandewale MC, Kumbhare RM (2018) Contemporary progress in the synthesis and reactions of 2-aminobenzothiazole: a review. New J Chem 42(2):776–797

38. Ding Y-S, Zheng Y-Z (2021) Anisotropic magnetocaloric effect in a dysprosium (III) single-molecule magnet—Commemorating the 100th anniversary of the birth of Academician Guangxian Xu. Journal of Rare Earths
39. Egorova A, Jackson M, Gavrilyuk V, Makarov V (2021) Pipeline of anti-Mycobacterium abscessus small molecules: Repurposable drugs and promising novel chemical entities. Medicinal research reviews
40. Ekennia AC, Osowole AA, Olasunkanmi LO, Onwudiwe DC, Ebenso EE (2017) Coordination behaviours of new (bidentate N, O-chelating) Schiff bases towards copper (II) and nickel (II) metal ions: synthesis, characterization, antimicrobial, antioxidant, and DFT studies. Res Chem Intermed 43(7):3787–3811
41. El-Boraey HA, El-Domiaty AM (2021) Influences of γ-ray irradiation on physico-chemical, structural, X-ray diffraction, thermal and antimicrobial activity of some γ-irradiated N', N'''-((Z)-ethane-1, 2-diylidine) bis (2-aminobenzohydrazide) metal complexes. Appl Radiat Isot 174:109774
42. French HS (1944) Magnetochemistry (Selwood, Pierce W.). ACS Publications
43. Gao F, Yang P, Xie J, Wang H (1995) Synthesis, characterization and antibacterial activity of novel Fe (III), Co (II), and Zn (II) complexes with norfloxacin. J Inorg Biochem 60(1):61–67
44. Gasparini LS, Macedo ND, Pimentel EF, Fronza M, Junior VL, Borges WS, Cole ER, Andrade TU, Endringer DC, Lenz D (2017) In vitro cell viability by CellProfiler® software as equivalent to MTT assay. Pharmacognosy magazine 13(Suppl 2):S365
45. Ha S-T, Koh T-M, Ong S-T, Lee T-L, Sivasothy Y (2009) Synthesis of 2-(4-Propyloxyphenyl) benzothiazole. Molbank 2009 (3):M609
46. Habeeb HA, Al-Adilee KJ, Jaber SA (2014) Synthesis, characterization, thermal and kinetic photo chemical decomposition study of new azo dye 7-[2-(BenzImidazolyl) Azo]-8-Hydroxy quinoline and its znic (II) complex. Synthesis 6:8
47. Harisha S, Keshavayya J, Prasanna S, Hoskeri HJ (2020) Synthesis, characterization, pharmacological evaluation and molecular docking studies of benzothiazole azo derivatives. J Mol Struct 1218:128477
48. Harris JB, Eldridge ML, Sayler G, Menn FM, Layton AC, Baudry J (2014) A computational approach predicting CYP450 metabolism and estrogenic activity of an endocrine disrupting compound (PCB-30). Environ Toxicol Chem 33(7):1615–1623
49. Hillier SL (1993) Diagnostic microbiology of bacterial vaginosis. Am J Obstet Gynecol 169(2):455–459
50. Ibrahim HM, Arafa WAA, Behbehani H (2018) L-Proline catalyzed one-pot synthesis of polysubstituted pyridine system incorporating benzothiazole moiety via sustainable sonochemical approach. RSC Adv 8(66):37606–37617
51. İnci D, Aydın R, Zorlu Y (2021) Cu (ii) complex with auxin (3-indoleacetic acid) and an aromatic planar ligand: synthesis, crystal structure, biomolecular interactions and radical scavenging activity.European Biophysics Journal:1–15
52. Jaber SA, Kyhoiesh HA, Jawad SH, Synthesis (2021) Characterization and Biological Activity Studies of Cadmium (II) Complex Derived from Azo Ligand 2-[2\-(5-Bromo Thiazolyl) Azo]-5-Dimethyl Amino Benzoic Acid. In: Journal of Physics: Conference Series, vol 1. IOP Publishing, p 012013
53. Johnatty SE, Pesaran T, Dolinsky J, Yussuf A, LaDuca H, James PA, O'Mara TA, Spurdle AB (2021) Case–case analysis addressing ascertainment bias for multigene panel testing implicates BRCA1 and PALB2 in endometrial cancer. Human Mutation
54. Joshi P, Kumar D (2014) Metal complexes of biological active 2-aminothiazole derived ligands. Russ J Coord Chem 40(7):445–459
55. Jovanović S, Petrović B, Bugarčić ŽD (2010) UV-Vis, HPLC, and 1H-NMR studies of the substitution reactions of some Pt (IV) complexes with 5'-GMP and L-histidine. J Coord Chem 63(14–16):2419–2430
56. Kaur H, Kumar S, Singh I, Saxena K, Kumar A (2010) Synthesis, characterization and biological activity of various substituted benzothiazole derivatives. Dig J Nanomater Bios 5:67–76
57. Khokra SL, Arora K, Mehta H, Aggarwal A, Yadav M (2011) Common methods to synthesize benzothiazole derivatives and their medicinal significance. International Journal of Pharmaceutical Sciences and Research 2(6):1356–1378
58. Kim D-H, Kwak Y, Kim ND, Sim T (2016) Antitumor effects and molecular mechanisms of ponatinib on endometrial cancer cells harboring activating FGFR2 mutations. Cancer Biol Ther 17(1):65–78
59. Kumar P, Nagarajan A, Uchil PD (2018) Analysis of cell viability by the MTT assay. Cold spring harbor protocols 2018 (6):pdb. prot095505
60. Kyhoiesh HAK, Al-Adilee KJ (2021) Synthesis, spectral characterization, antimicrobial evaluation studies and cytotoxic activity of some transition metal complexes with tridentate (N, N, O) donor azo dye ligand. Results in Chemistry 3:100245
61. Kyhoiesh HAK, Al-Hussainawy MK, Waheeb AS, Al-Adilee KJ (2021) Synthesis, spectral characterization, lethal dose (LD 50) and acute toxicity studies of 1, 4-Bis (imidazolylazo) benzene (BIAB). Heliyon:e07969
62. Liu D, Enriquez L, Ford CE (2021) ROR2 Is Epigenetically Regulated in Endometrial Cancer. Cancers 13(3):383
63. Liu J, Wen Y, Gao L, Gao L, He F, Zhou J, Wang J, Dai R, Chen X, Kang D (2020) Design, synthesis and biological evaluation of novel 1 H-1, 2, 4-triazole, benzothiazole and indazole-based derivatives as potent FGFR1 inhibitors via fragment-based virtual screening. J Enzyme Inhib Med Chem 35(1):72–84
64. Liu J, Wu B-w, Zhang B, Liu Y (2006) Synthesis and characterization of metal complexes of Cu (II), Ni (II), Zn (II), Co (II), Mn (II) and Cd (II) with tetradentate Schiff bases. Turk J Chem 30(1):41–48
65. Loffredo J, Tommarello D, Abulez T, Ao W, Teng P-n, Conrads K, Litzi T, Hood B, Soltis A, Dalgard C (2021) Integrated multi-omic analyses reveals clinical relevance of endometrial cancer cell line models. Gynecol Oncol 162:S11
66. Manju KD, Kumar D (2011) Cadmium and tin complexes of Schiff-base ligands. J Coord Chem 64(12):2130–2156
67. Marks DC, Belov L, Davey MW, Davey RA, Kidman AD (1992) The MTT cell viability assay for cytotoxicity testing in multidrug-resistant human leukemic cells. Leuk Res 16(12):1165–1173

68. Mavroidi B, Sagnou M, Stamatakis K, Paravatou-Petsotas M, Pelecanou M, Methenitis C (2016) Palladium (II) and platinum (II) complexes of derivatives of 2-(4'-aminophenyl) benzothiazole as potential anticancer agents. Inorg Chim Acta 444:63–75
69. Meyer AS Jr, Ayres GH (1957) The Mole Ratio Method for Spectrophotometric Determination of Complexes in Solution1. J Am Chem Soc 79(1):49–53
70. Mignani S, Majoral J-P, Desaphy J-F, Lentini G (2020) From Riluzole to Dexpramipexole via Substituted-Benzothiazole Derivatives for Amyotrophic Lateral Sclerosis Disease Treatment: Case Studies. Molecules 25(15):3320
71. Milacic V, Dou QP (2009) The tumor proteasome as a novel target for gold (III) complexes: implications for breast cancer therapy. Coord Chem Rev 253(11–12):1649–1660
72. Mishra A, Batar A, Kumar R, Khandelwal A, Lama P, Chhabra M, Metre RK (2021) Assembly of Di-, Tetra-and Hexanuclear Organostannoxanes Using Hemi Labile Intramolecular N→ Sn Coordination: Synthesis, Structure, DFT and Antibacterial Studies. Polyhedron 209:115487
73. Mustapha S, Ndamitso M, Abdulkareem A, Tijani J, Shuaib D, Mohammed A, Sumaila A (2019) Comparative study of crystallite size using Williamson-Hall and Debye-Scherrer plots for ZnO nanoparticles. Adv Nat Sci NanoSci NanoTechnol 10(4):045013
74. Parisi OI, Aiello D, Casula MF, Puoci F, Malivindi R, Scrivano L, Testa F (2016) Mesoporous nanocrystalline tio 2 loaded with ferulic acid for sunscreen and photo-protection: Safety and efficacy assessment. RSC Adv 6(87):83767–83775
75. Pestov A, Nazirov A, Modin E, Mironenko A, Bratskaya S (2015) Mechanism of Au (III) reduction by chitosan: Comprehensive study with 13C and 1H NMR analysis of chitosan degradation products. Carbohydr Polym 117:70–77
76. Pitchumani Violet Mary C, Shankar R, Vijayakumar S (2019) Theoretical insights into the metal chelating and antimicrobial properties of the chalcone based Schiff bases. Mol Simul 45(8):636–645
77. Prajapat P (2012) Importance of Benzothiazole Motif in Modern Drug Discovery: Introduction. Organic Chemistry 8(2):1795–1801
78. Pramanik HA, Paul PC, Mondal P, Bhattacharjee CR (2015) Mixed ligand complexes of cobalt (III) and iron (III) containing N2O2-chelating Schiff base: Synthesis, characterisation, antimicrobial activity, antioxidant and DFT study. J Mol Struct 1100:496–505
79. Purushotham K, Nandeeshwar P, Srikanth I, Ramanjaneyulu K, Himabindhu J (2019) Phytochemical Screening and In-Vitro Antioxidant activity of Senna occidentalis. Research Journal of Pharmacy and Technology 12(2):549–552
80. Radisavljević S, Petrović B (2020) Gold (III) Complexes: An Overview on Their Kinetics, Interactions With DNA/BSA, Cytotoxic Activity, and Computational Calculations. Front Chem 8:379
81. Roy FE, Berteau T, Bestman-Smith J, Grandjean Lapierre S, Dufresne SF, Domingo M-C, Leduc J-M (2021) Validation of a Gradient Diffusion Method (Etest®) for Antimicrobial Susceptibility Testing of Aerococcus urinae to Fluoroquinolones.Journal of Clinical Microbiology:JCM.00259–00221
82. Sabir S, Malik b A, Iftikhar K (1994) Studies on the Thermal Stability of Cu (I) and Ag (I) Complexes-II. Mixed-Ligand Complexes of CuI and AgI with Thiourea and Heterocyclic Amines. Synthesis and Reactivity in Inorganic and Metal-Organic Chemistry. 24:1377–13968
83. Sagdinc S, Köksoy B, Kandemirli F, Bayari SH (2009) Theoretical and spectroscopic studies of 5-fluoro-isatin-3-(N-benzylthiosemicarbazone) and its zinc (II) complex. J Mol Struct 917(2–3):63–70
84. Serafińczuk J, Moszak K, Pawlaczyk Ł, Olszewski W, Pucicki D, Kudrawiec R, Hommel D (2020) Determination of dislocation density in GaN/sapphire layers using XRD measurements carried out from the edge of the sample. J Alloys Compd 825:153838
85. Singh M, Singh SK (2014) Benzothiazoles: how relevant in cancer drug design strategy? Anti-Cancer Agents in Medicinal Chemistry (Formerly Current Medicinal Chemistry-Anti-Cancer Agents). 14:127–1461
86. Sirajuddin M, Ali S (2016) Organotin (IV) carboxylates as promising potential drug candidates in the field of cancer chemotherapy. Curr Pharm Design 22(44):6665–6681
87. Soliman MH, Mohamed GG (2013) Cr (III), Mn (II), Fe (III), Co (II), Ni (II), Cu (II) and Zn (II) new complexes of 5-aminosalicylic acid: spectroscopic, thermal characterization and biological activity studies. Spectrochim Acta Part A Mol Biomol Spectrosc 107:8–15
88. Stankovic AS, Kasalovic MP, Bukonjic AM, Mijajlovic MZ, Tomovic DL, Nikolic MV (2019) Biological Activity of Au (III) Complexes. Serbian Journal of Experimental and Clinical Research
89. Sulimov VB, Kutov DC, Taschilova AS, Ilin IS, Tyrtyshnikov EE, Sulimov AV (2021) Docking paradigm in drug design. Curr Top Med Chem 21(6):507–546
90. Sun RW-Y, Ma D-L, Wong EL-M, Che C-M (2007) Some uses of transition metal complexes as anti-cancer and anti-HIV agents.Dalton Transactions(43):4884–4892
91. Sun Y, Lu Y, Bian M, Yang Z, Ma X, Liu W (2021) Pt (II) and Au (III) complexes containing Schiff-base ligands: A promising source for antitumor treatment. Eur J Med Chem 211:113098
92. Tamer Ö, Mahmoody H, Feyzioğlu KF, Kılınç O, Avci D, Orun O, Dege N, Atalay Y (2020) Synthesis of the first mixed ligand Mn (II) and Cd (II) complexes of 4-methoxy-pyridine-2-carboxylic acid, molecular docking studies and investigation of their anti-tumor effects in vitro. Appl Organomet Chem 34(3):e5416
93. Tang X, Wang Z, Zhong X, Wang X, Chen L, He M, Xue W (2019) Synthesis and biological activities of benzothiazole derivatives bearing a 1, 3, 4-thiadiazole moiety. Phosphorus, Sulfur, and Silicon and the Related Elements 194 (3):241-248
94. Turan N, Buldurun K, Adiguzel R, Aras A, Turkan F, Bursal E (2021) Investigation of spectroscopic, thermal, and biological properties of FeII, CoII, ZnII, and RuII complexes derived from azo dye ligand. J Mol Struct 1244:130989
95. Tyuftin AA, Mohammed H, Kerry JP, O'Sullivan MG, Hamill R, Kilcawley K (2021) Microscopy-assisted digital photography as an economical analytical tool for assessment of food particles and their distribution through the use of the ImageJ program. Advances in Nutrition and Food Science 2021 (2):1-10
96. Varghese AM, Patel J, Janjigian YY, Meng F, Selcuklu SD, Iyer G, Houck-Loomis B, Harding JJ, O'Reilly EM, Abou-Alfa GK (2021) Noninvasive detection of polyclonal acquired resistance to FGFR inhibition in patients with cholangiocarcinoma harboring FGFR2 alterations. JCO Precision Oncology 5:44–50

97. Venkatesh P, Pandeya S (2009) Synthesis, characterisation and anti-inflammatory activity of some 2-amino benzothiazole derivatives
98. Verma AK, Martin A, Singh Sr AK (2014) Synthesis, Characterization and evaluation of Anti-inflammatory and Analgesic activity of Benzothiazole derivatives. Indian Journal of Pharmaceutical and Biological Research 2(3):84
99. Vernack E, Costa D, Tingaut P, Marcus P (2020) DFT studies of 2-mercaptobenzothiazole and 2-mercaptobenzimidazole as corrosion inhibitors for copper. Corros Sci 174:108840
100. Waheeb AS, Al-Adilee KJ (2021) Synthesis, characterization and antimicrobial activity studies of new heterocyclic azo dye derived from 2-amino-4, 5-dimethyl thiazole with some metal ions. Materials Today: Proceedings 42:2150-2163
101. Wang P, Leung CH, Ma DL, Sun RWY, Yan SC, Chen QS, Che CM (2011) Specific blocking of CREB/DNA binding by cyclometalated platinum (II) complexes. Angew Chem 123(11):2602–2606
102. Watarai H, Chen J (2017) Magnetophoretic Mole-Ratio Method. Anal Chem 89(19):10141–10146
103. Ying X, Che X, Wang J, Zou G, Yu Q, Zhang X (2021) CDK1 serves as a novel therapeutic target for endometrioid endometrial cancer. J Cancer 12(8):2206

Figures

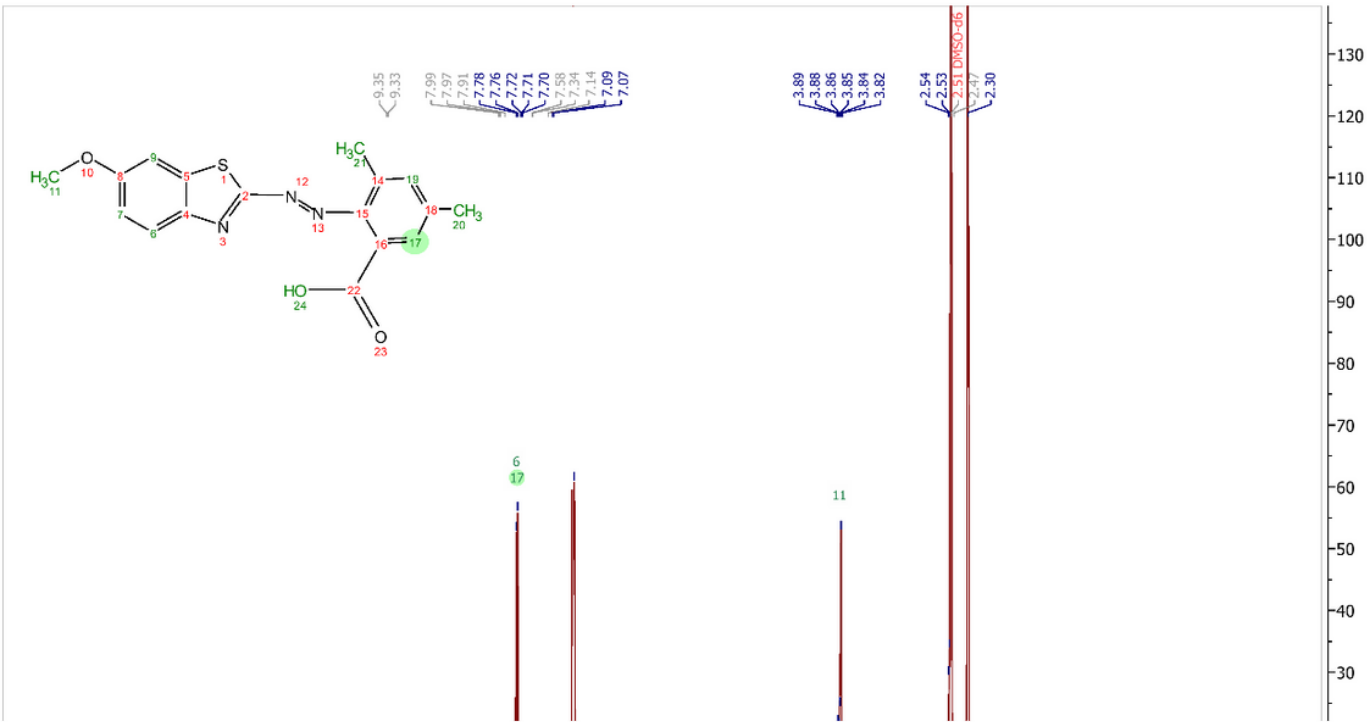

Figure 1

^{1}H NMR Spectrum of ligand (6-MBTAMB).

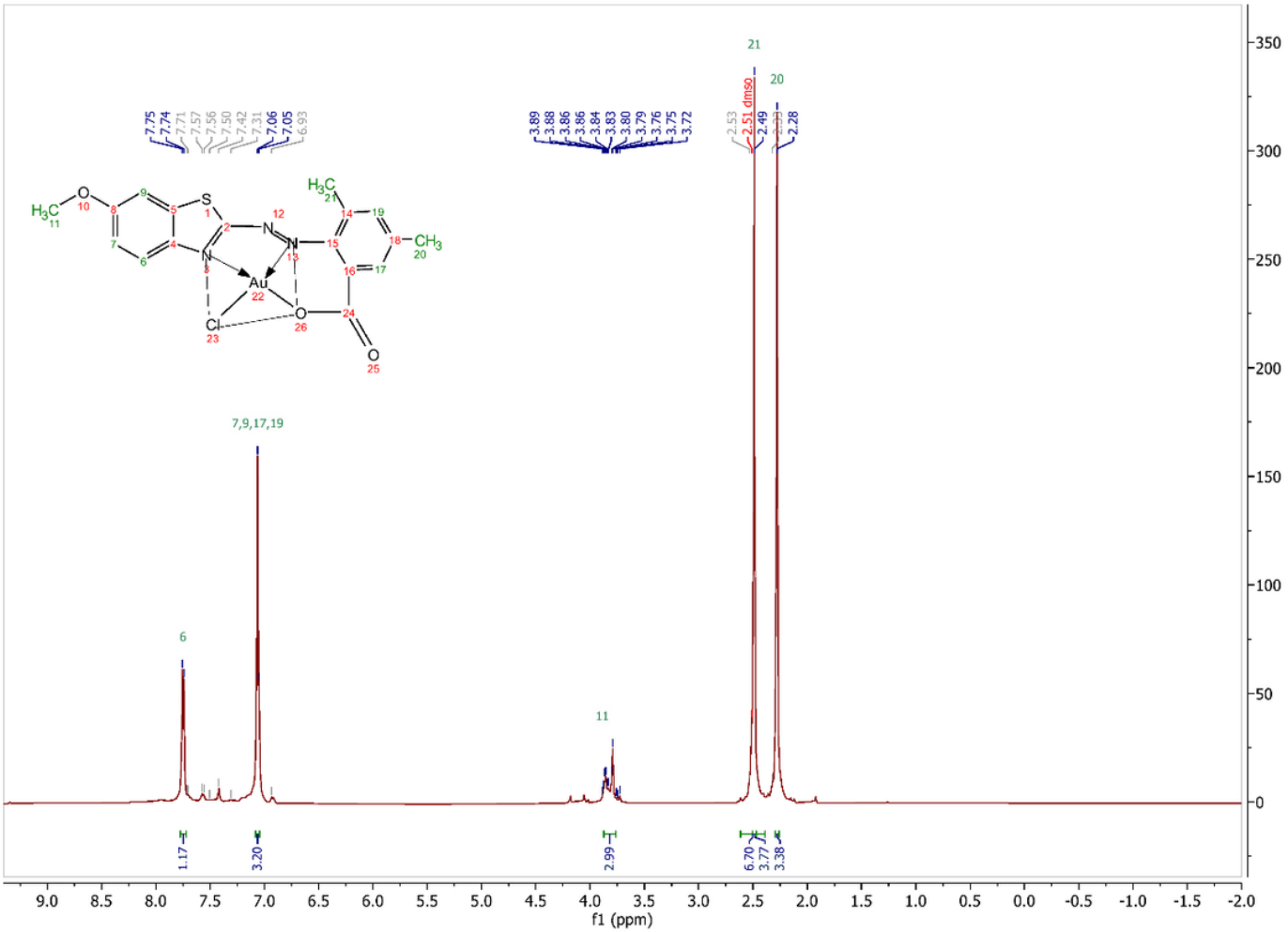

Figure 2

^{1}H NMR Spectrum of Au(III)-Complex.

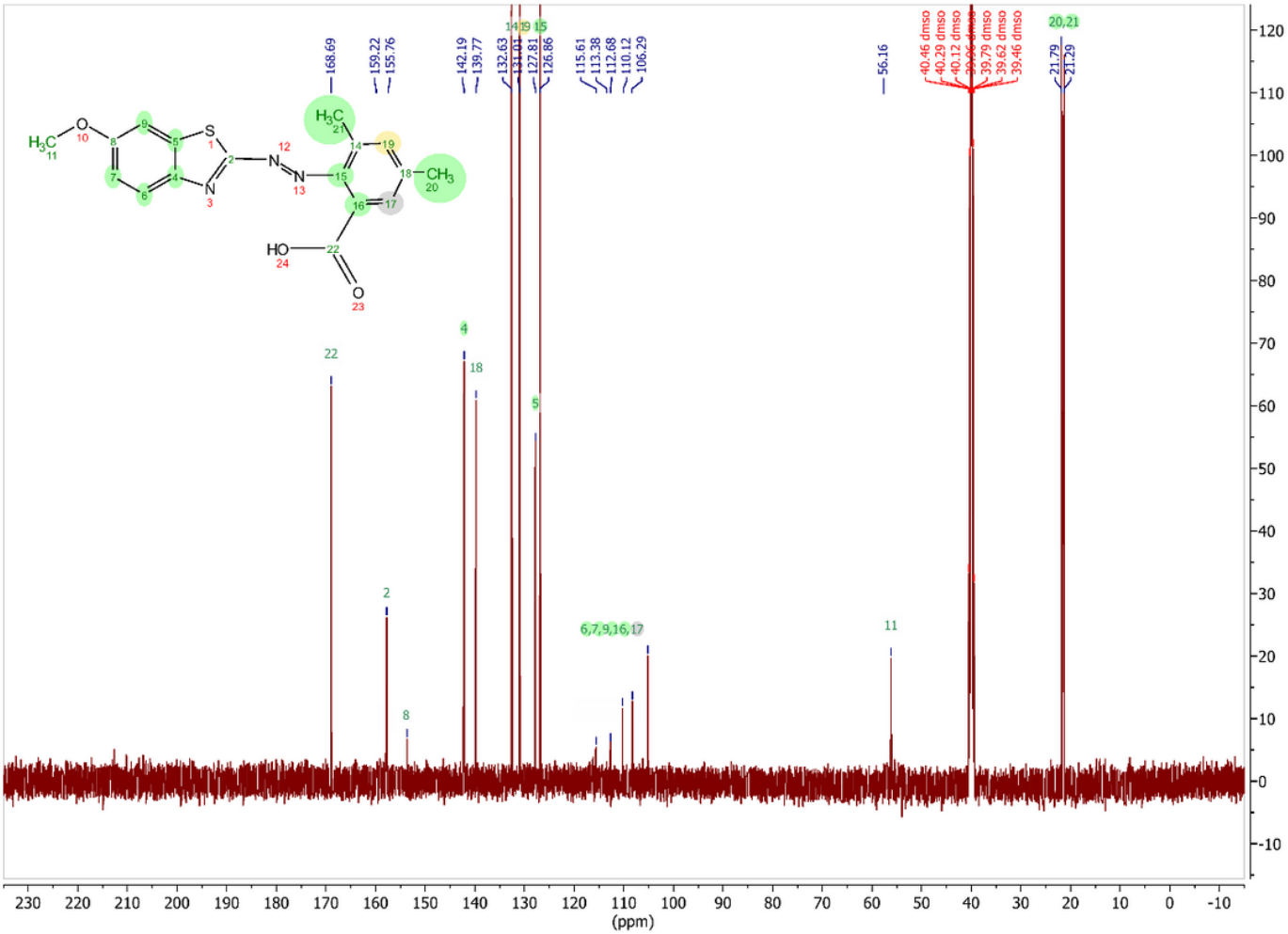

Figure 3

^{13}C NMR Spectrum of ligand (6-MBTAMB).

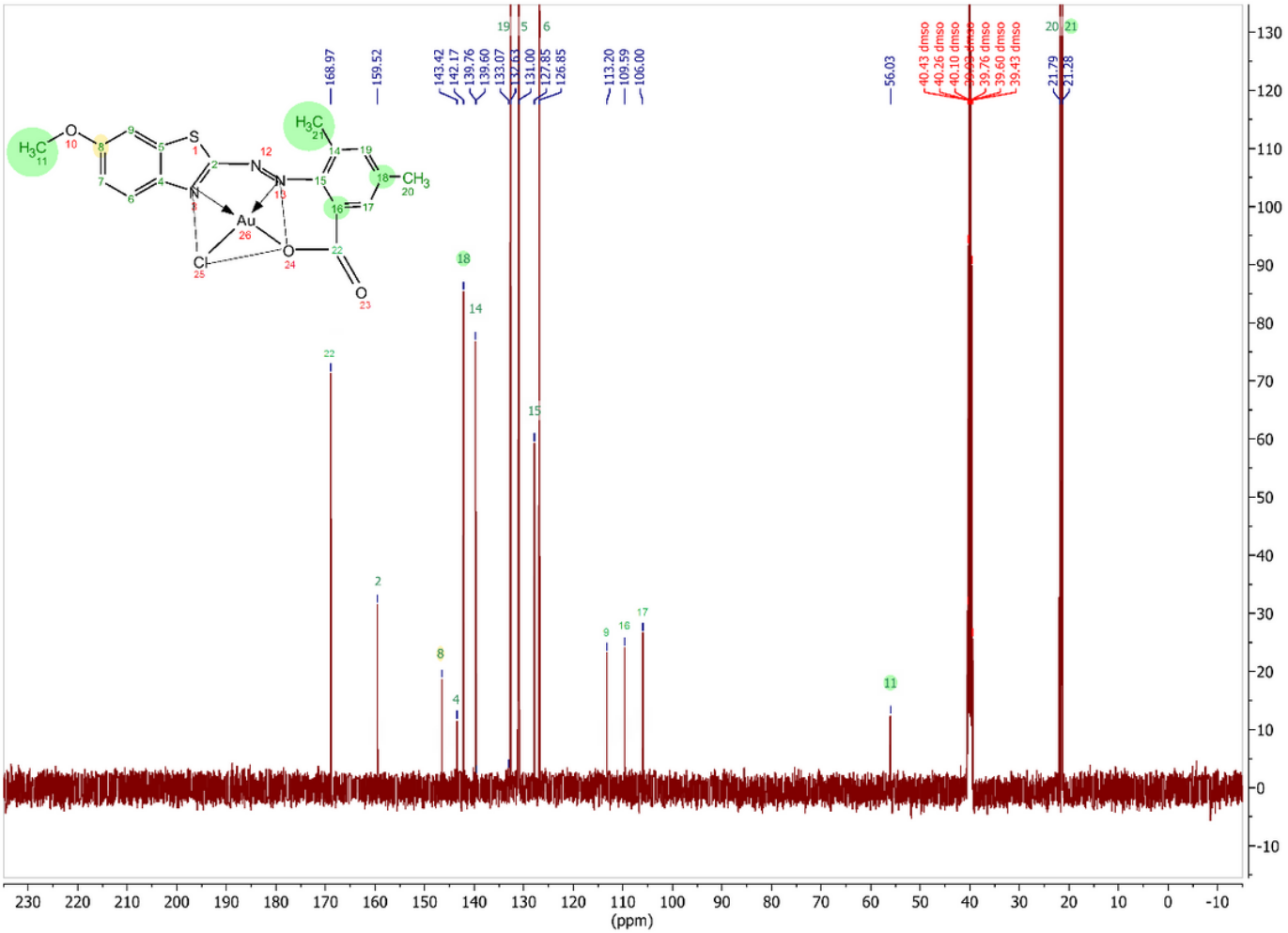

Figure 4

^{13}C NMR Spectrum of Au(III)-Complex.

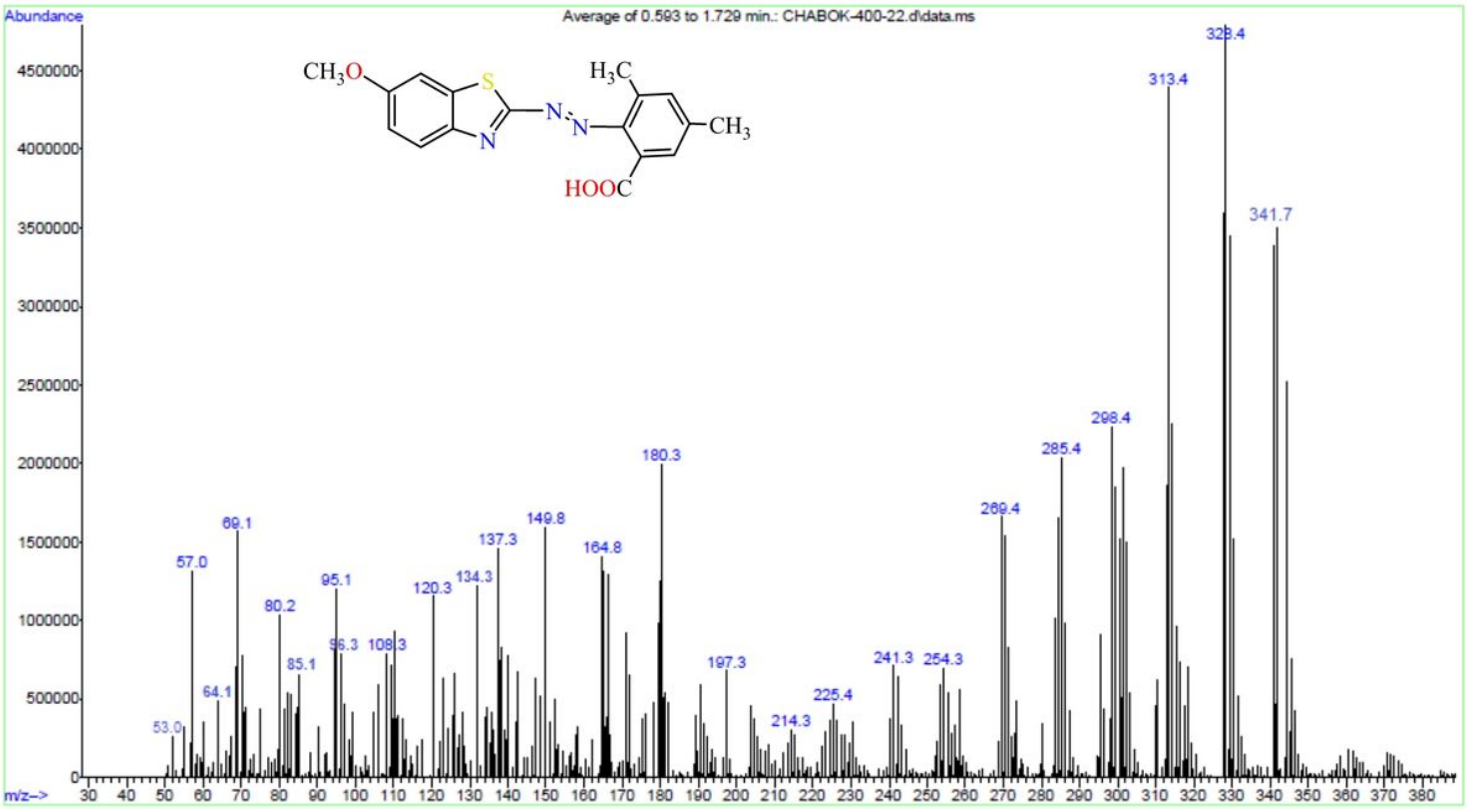

Figure 5

Mass spectrum of azo ligand (6-MBTAMB).

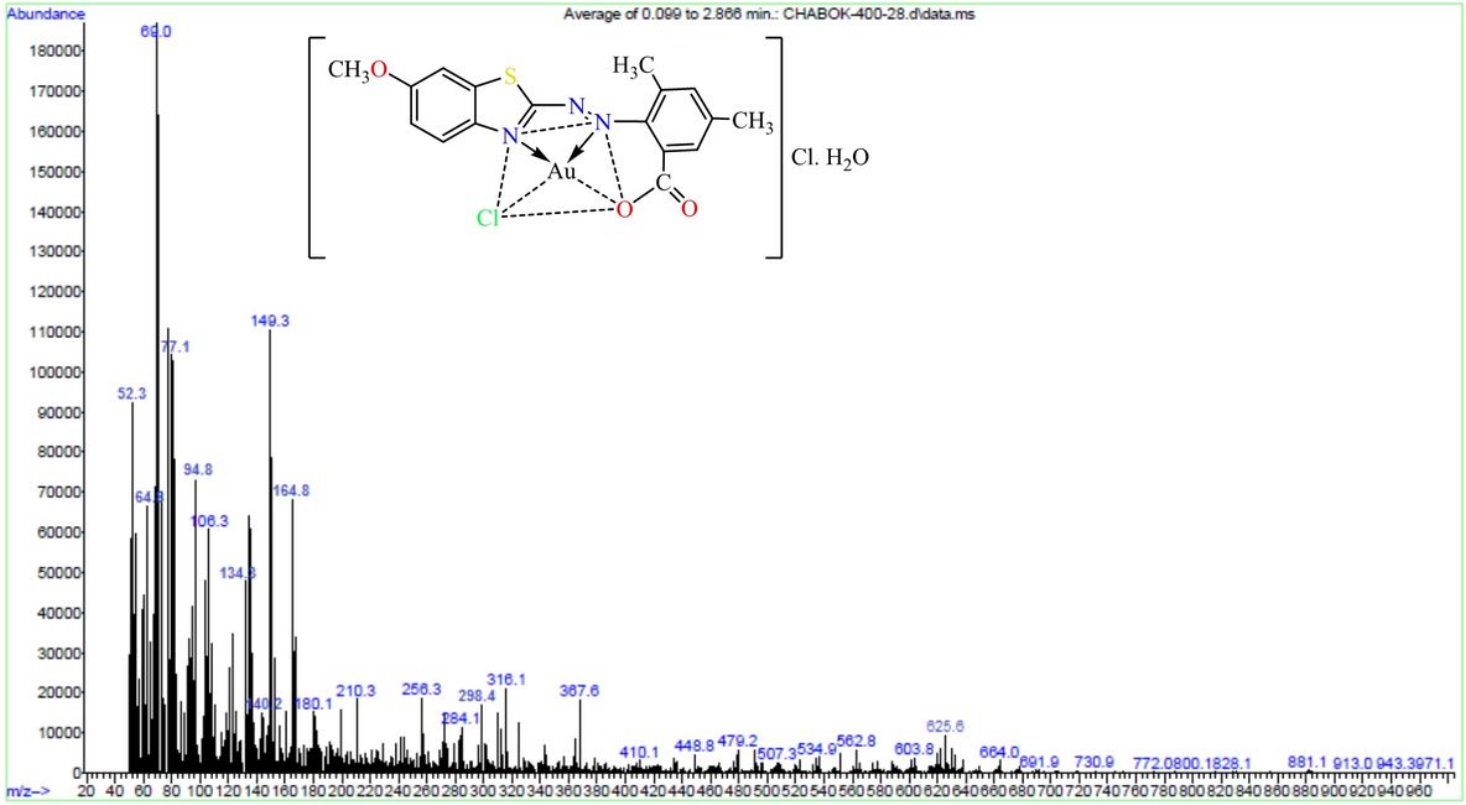

Figure 6

Mass spectrum for Au(III)-Complex.

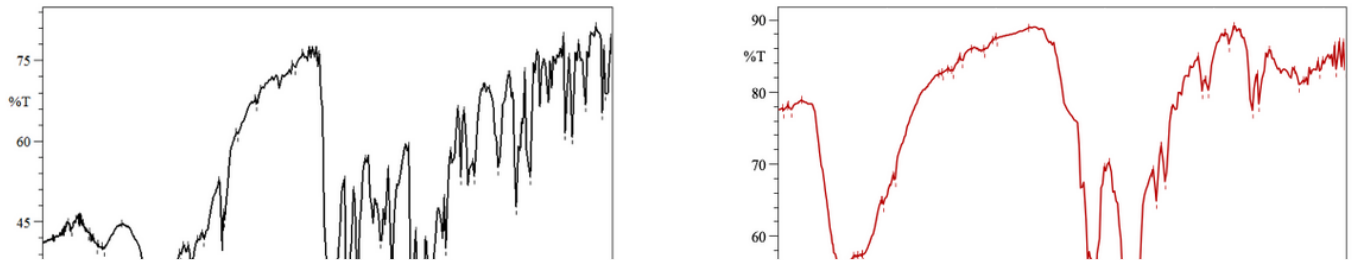

Figure 7

FT-IR spectrum of the ligand (6-MBTAMB) with metal complexes.

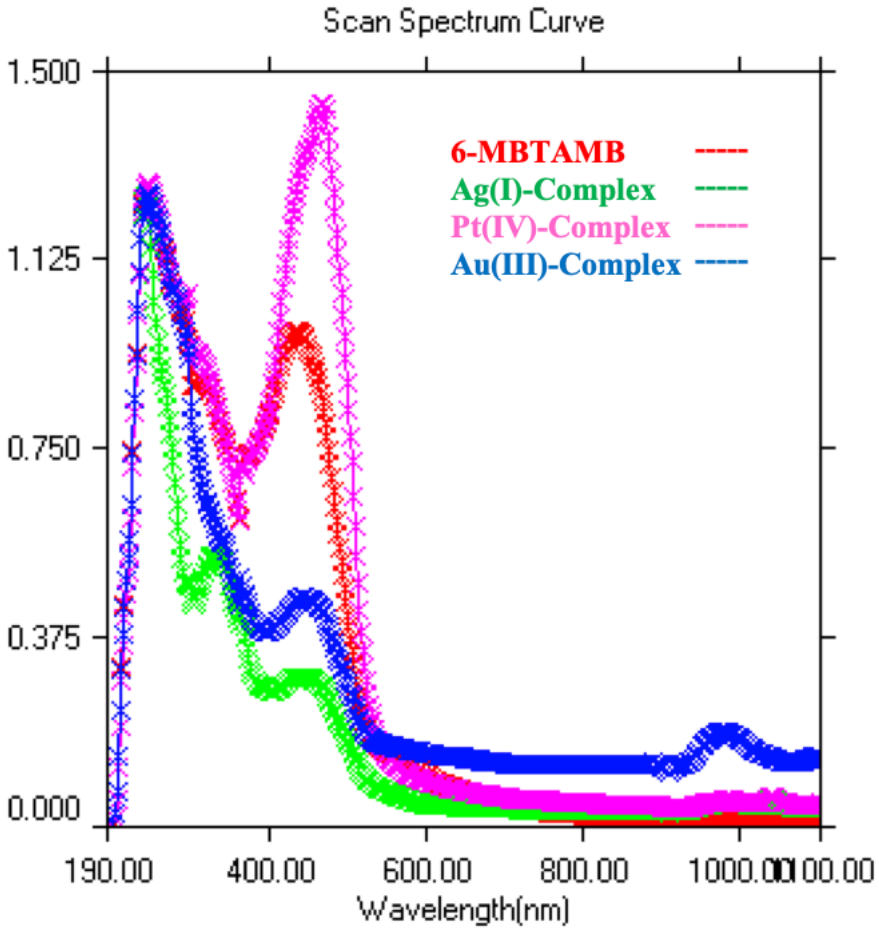

Figure 8

UV-Vis spectra of ligand (6-MBTAMB) and its chelates complexes.

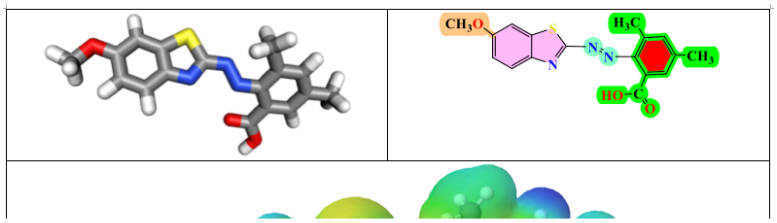

Figure 9

The suggested structure formula of (6-MBTAMB) and chelate complexes.

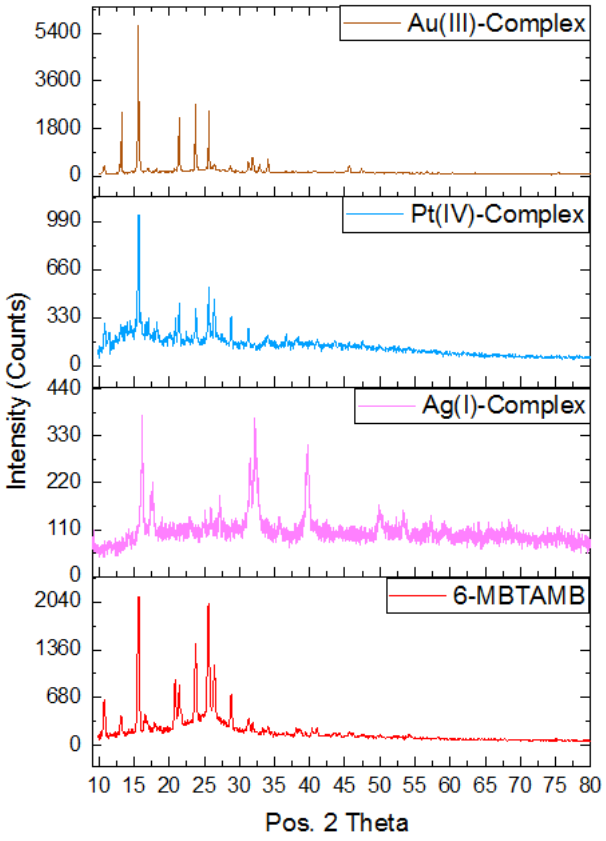

Figure 10

XRD patterns for ligand (6-MBTAMB) and chelate complexes.

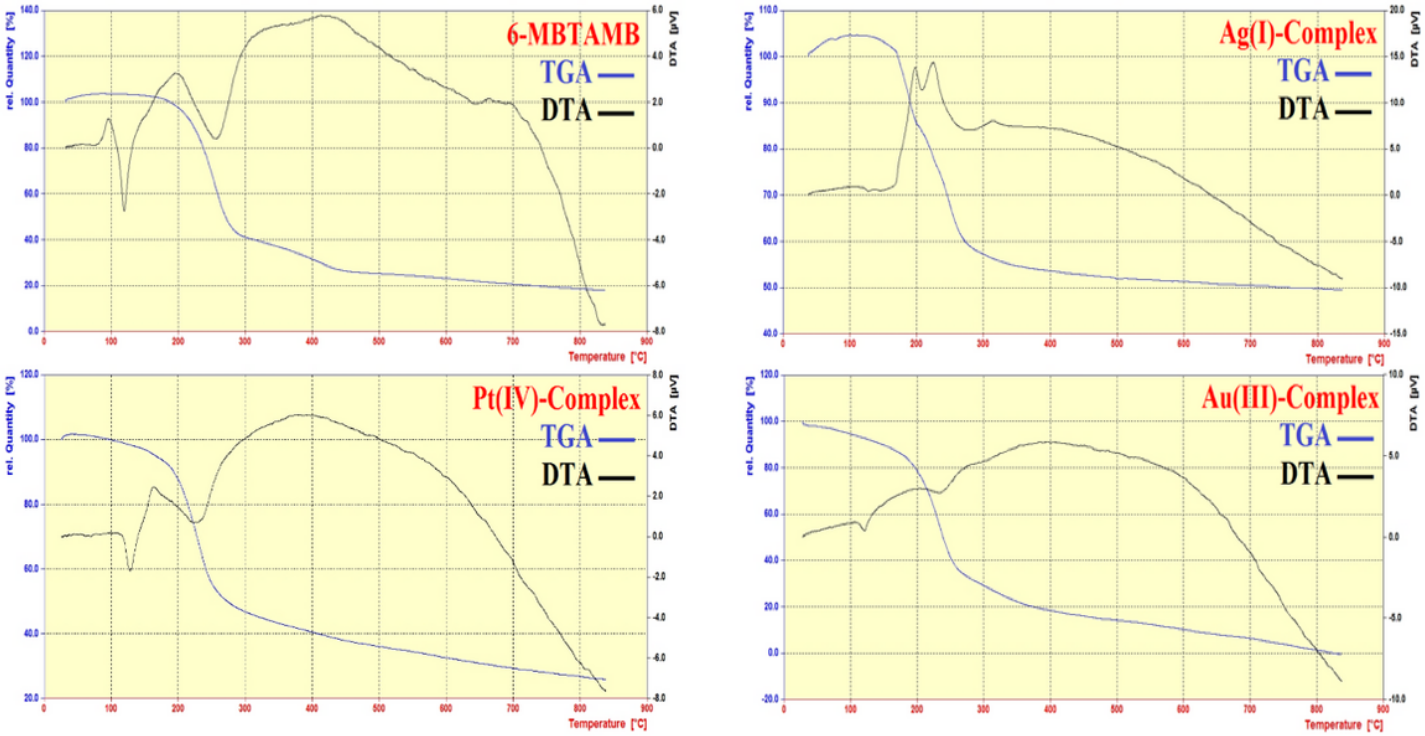

Figure 11

TG-DTA curves of ligand (6-MBTAMB) and chelate complexes.

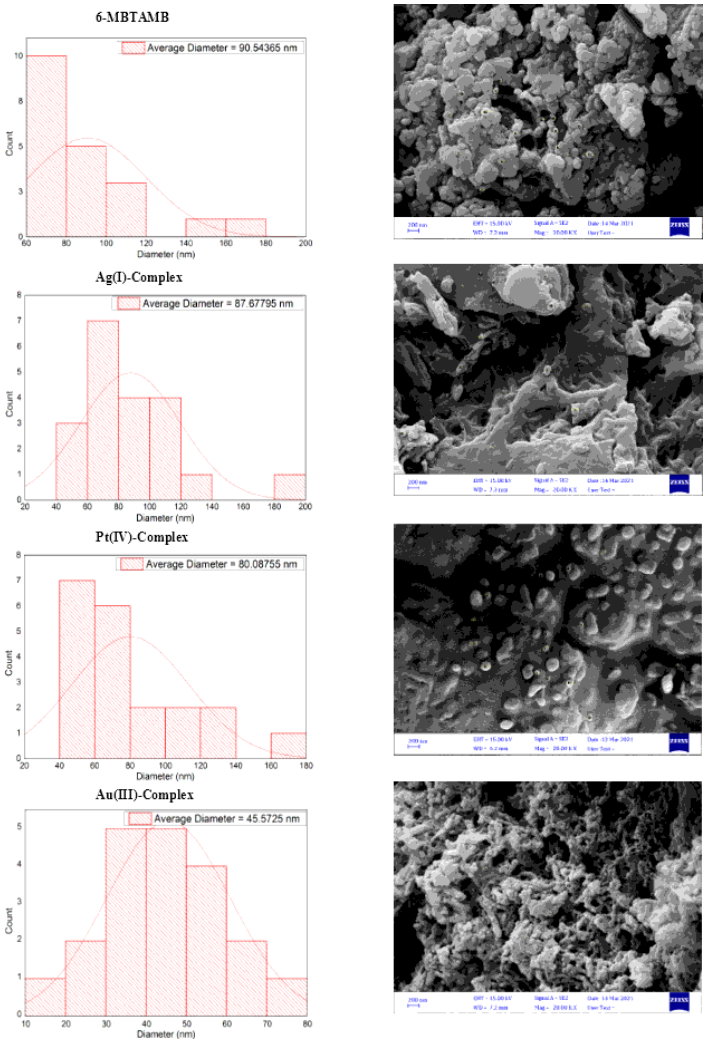

Figure 12

FE-SEM images of ligand (6-MBTAMB) and chelate complexes.

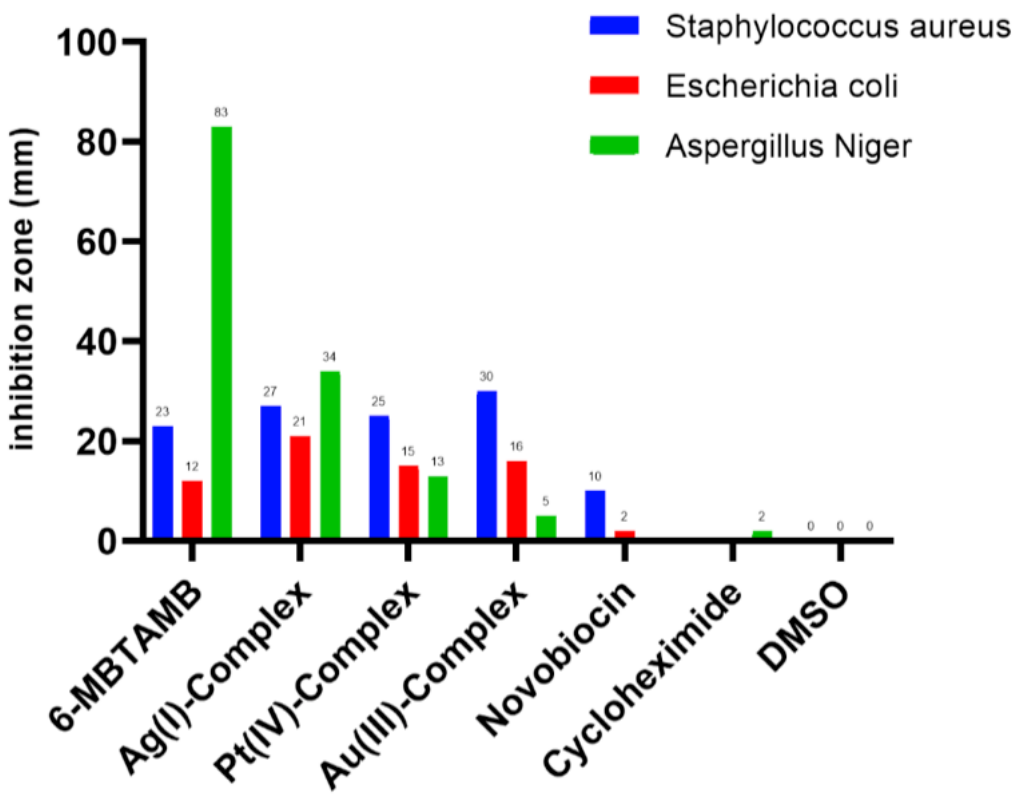

Figure 13

In vitro antimicrobial activity of ligand (6-MBTAMB) and its complexes.

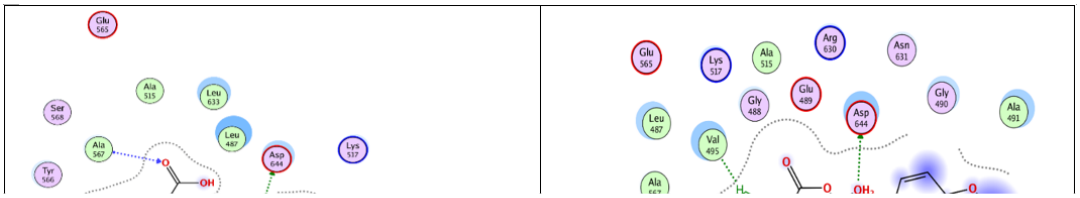

Figure 14

2D view of intermolecular interactions of FGFR2 protein (a) 6-MBTAMB, (b) Ag(I)-Complex, (c) Pt(IV)-Complex, (d) Au(III)-Complex.

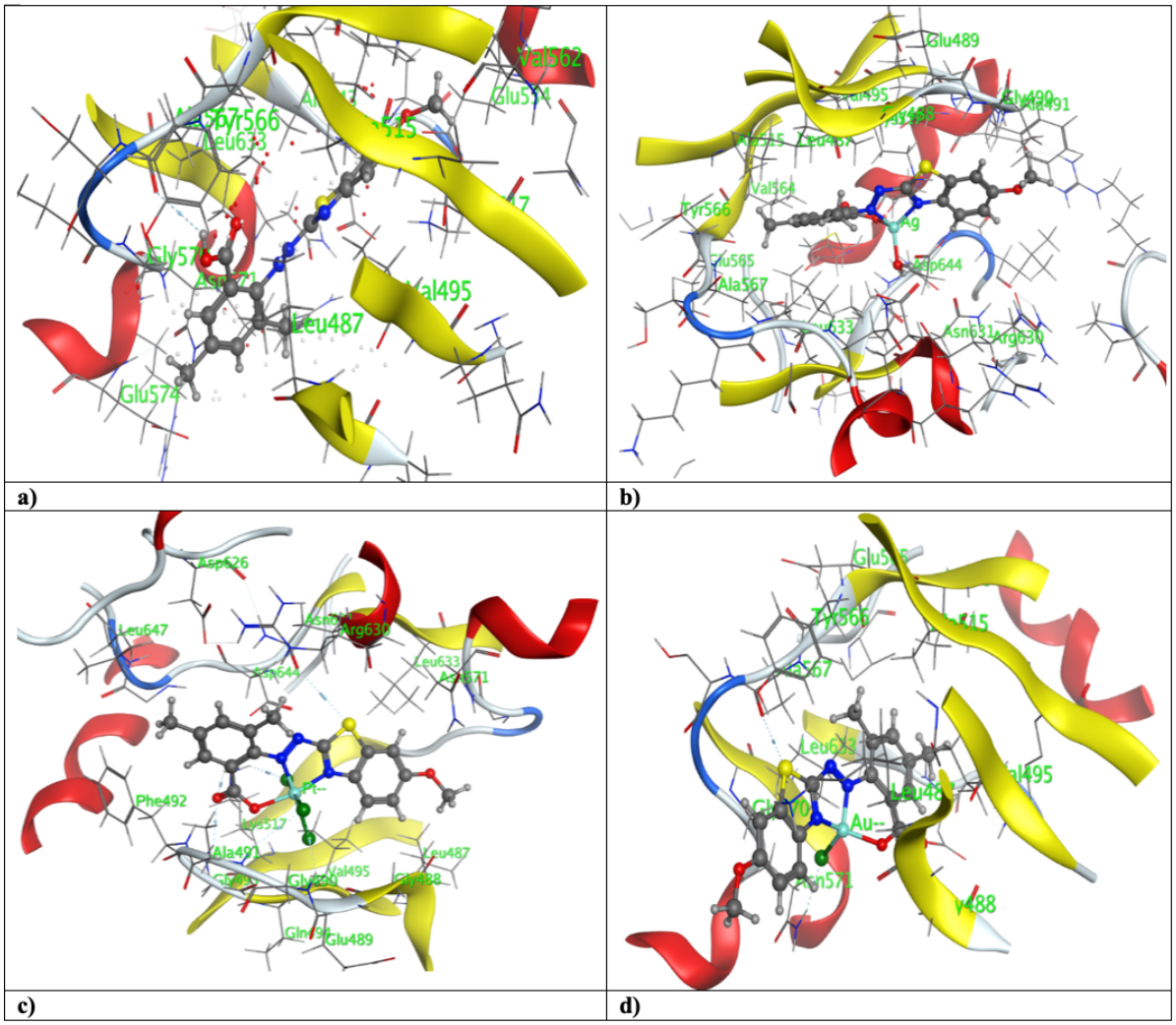

Figure 15

3D view of intermolecular interactions of FGFR2 protein (a) 6-MBTAMB, (b) Ag(I)-Complex, (c) Pt(IV)-Complex, (d) Au(III)-Complex.

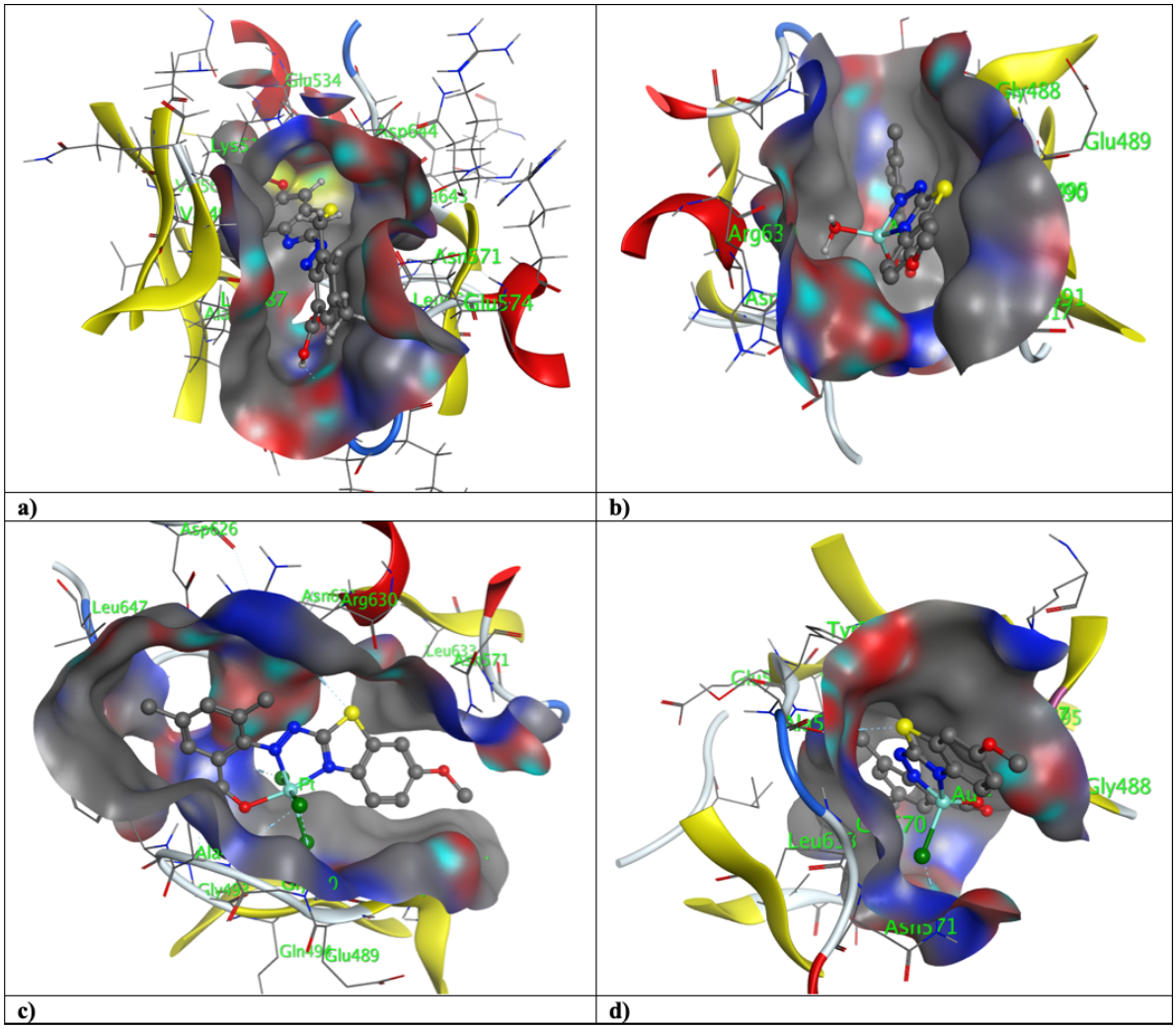

Figure 16

Isolated active site of FGFR2 protein (a) 6-MBTAMB, (b) Ag(I)-Complex, (c) Pt(IV)-Complex, (d) Au(III)-Complex.

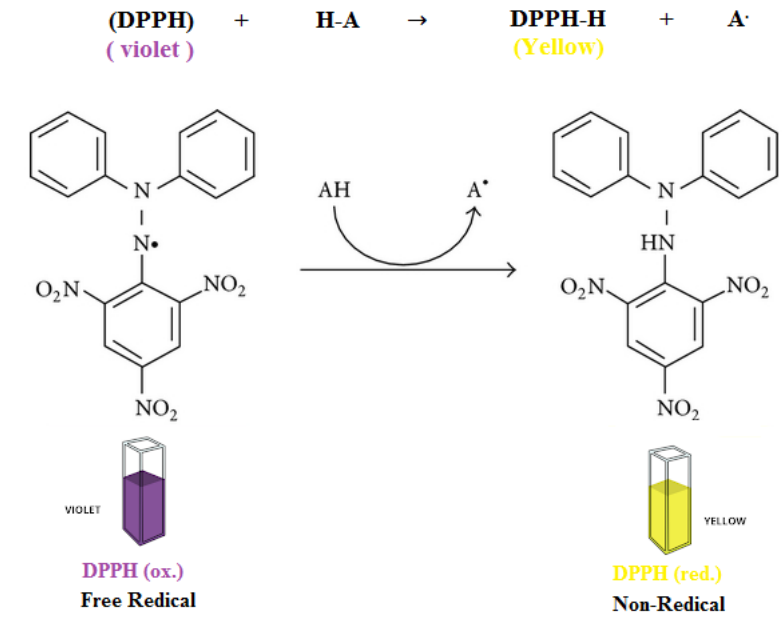

Figure 17

Mechanism of free radical scavenging activity.

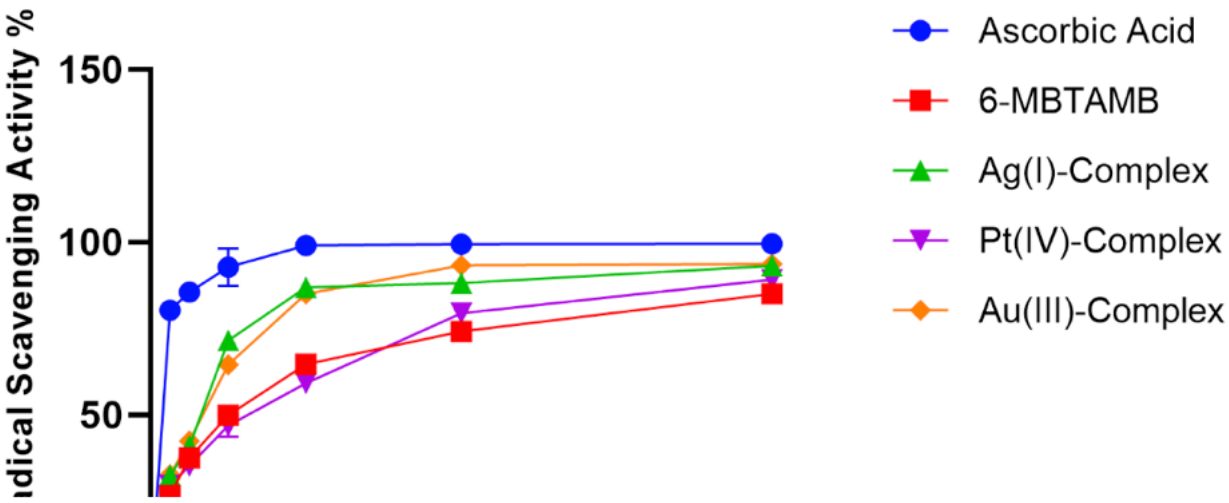

Figure 18

Antioxidant activities of synthesized compounds and positive controls.

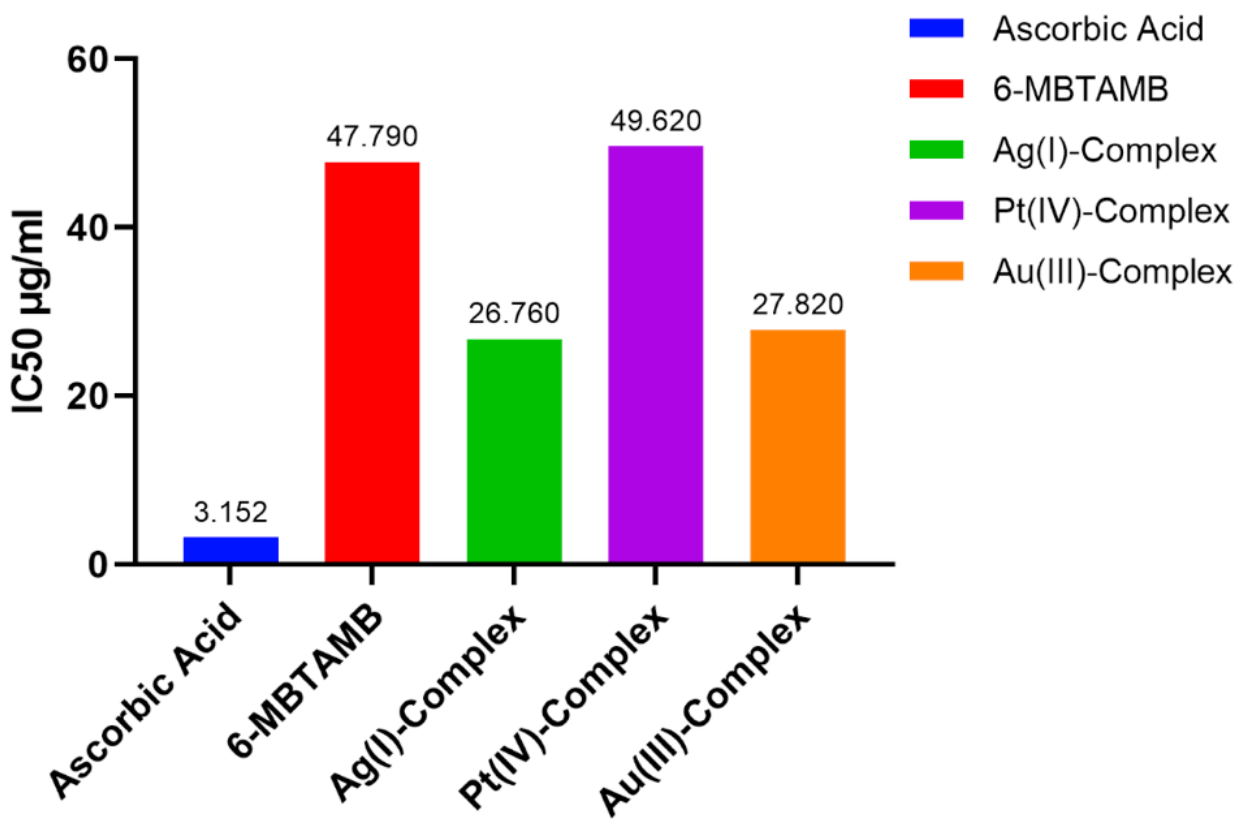

Figure 19

IC_{50} values of DPPH scavenging activity of ligand, complexes and ascorbic acid.

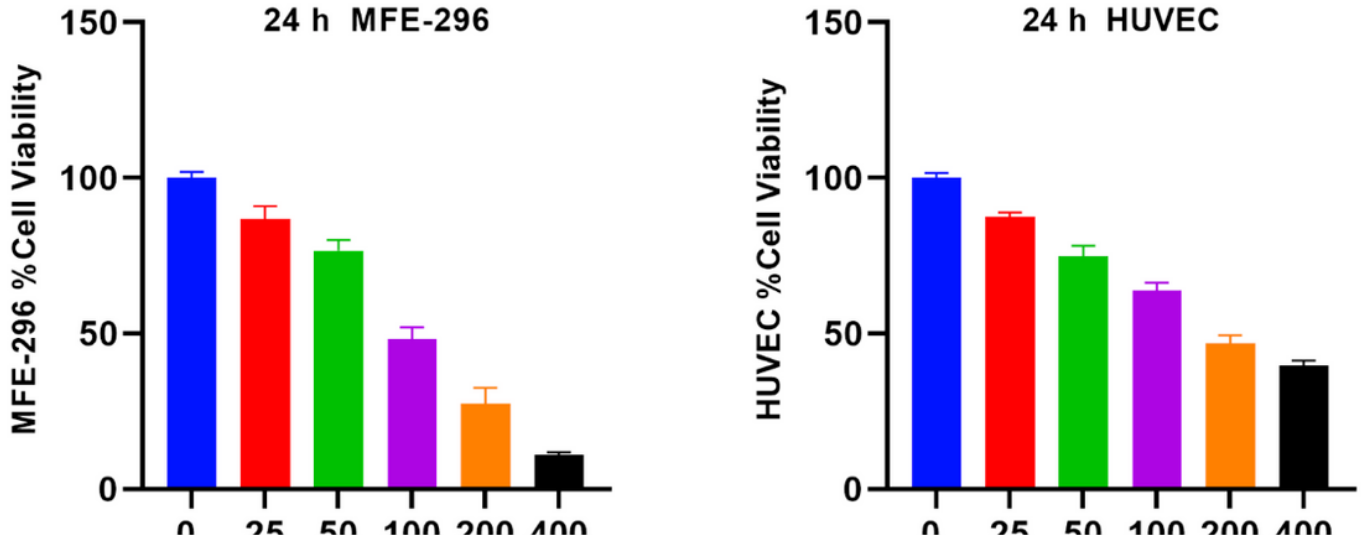

Figure 20

% Cell viability for ligand (6-MBTAMB) against endometrial cancer cells (MFE-296) and the normal cells (HUVEC).

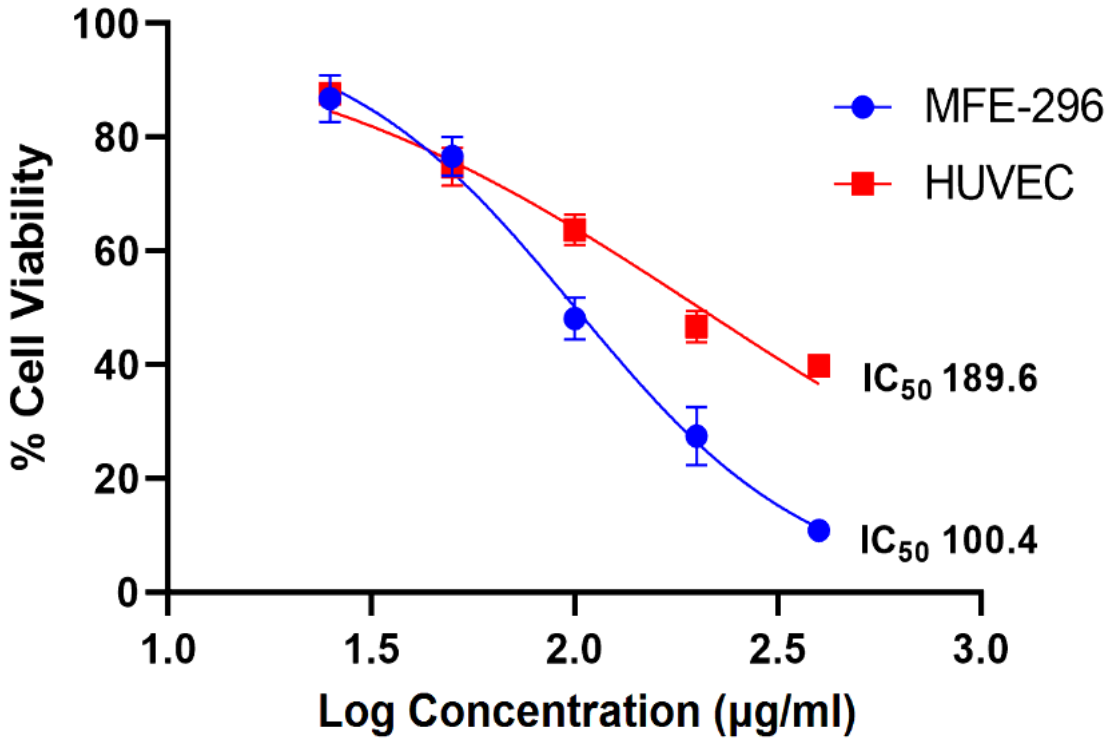

Figure 21

IC_{50} for ligand (6-MBTAMB) in (MFE-296) cell line and (HUVEC) natural cell line.

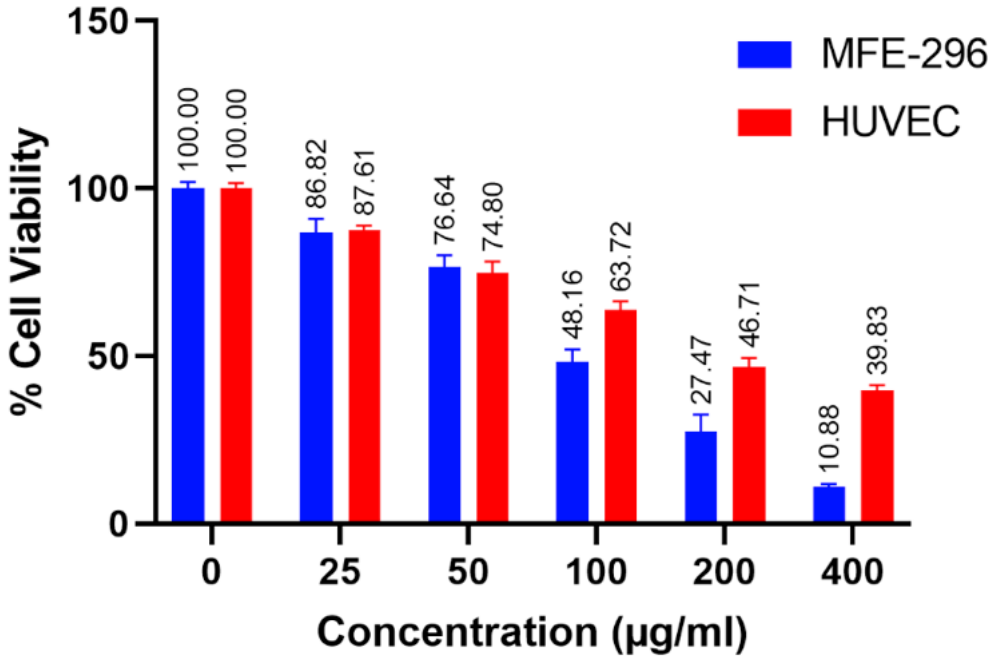

Figure 22

For ligand (6-MBTAMB) % viability, a comparison was made between carcinoma and natural cells

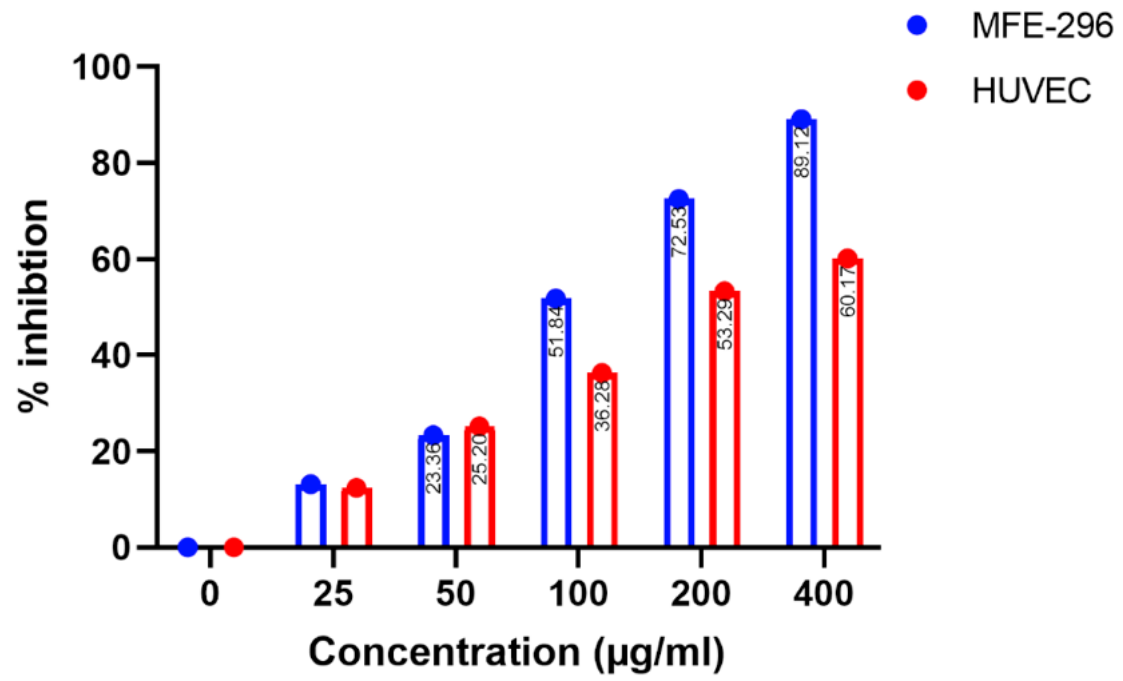

Figure 23

For ligand (6-MBTAMB) % inhibition, a comparison was made between carcinoma and natural cells.

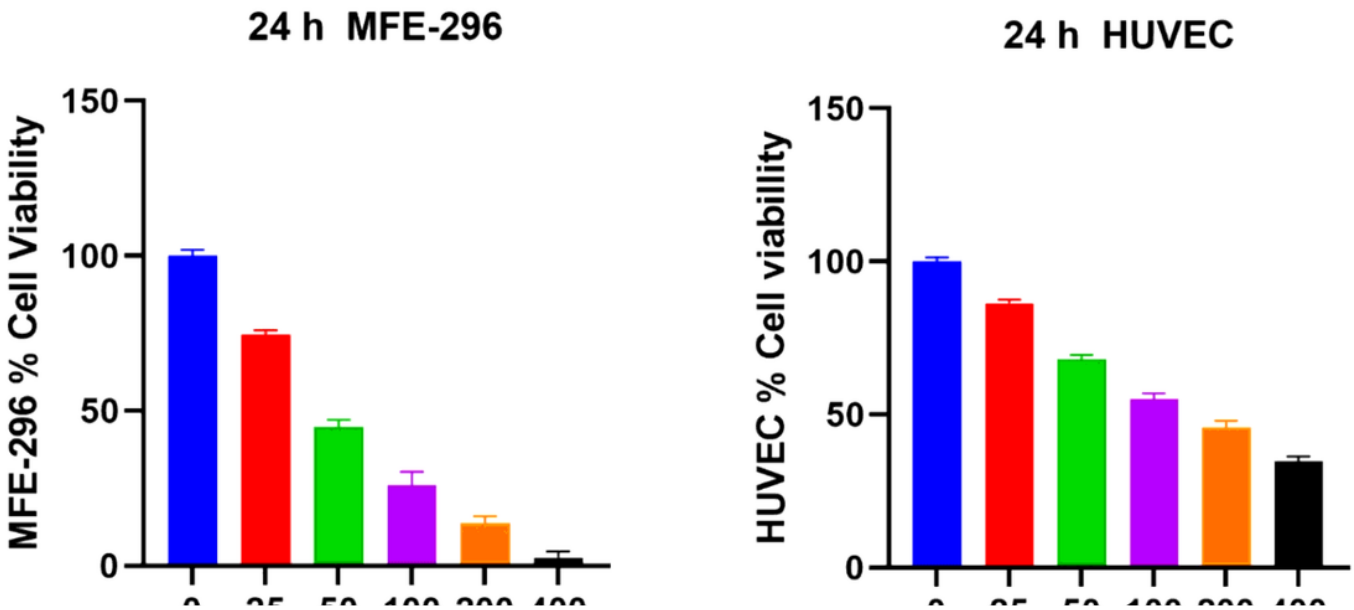

Figure 24

% Cell viability for Au(III)-Complex against endometrial cancer cells (MFE-296) and the normal cells (HUVEC).

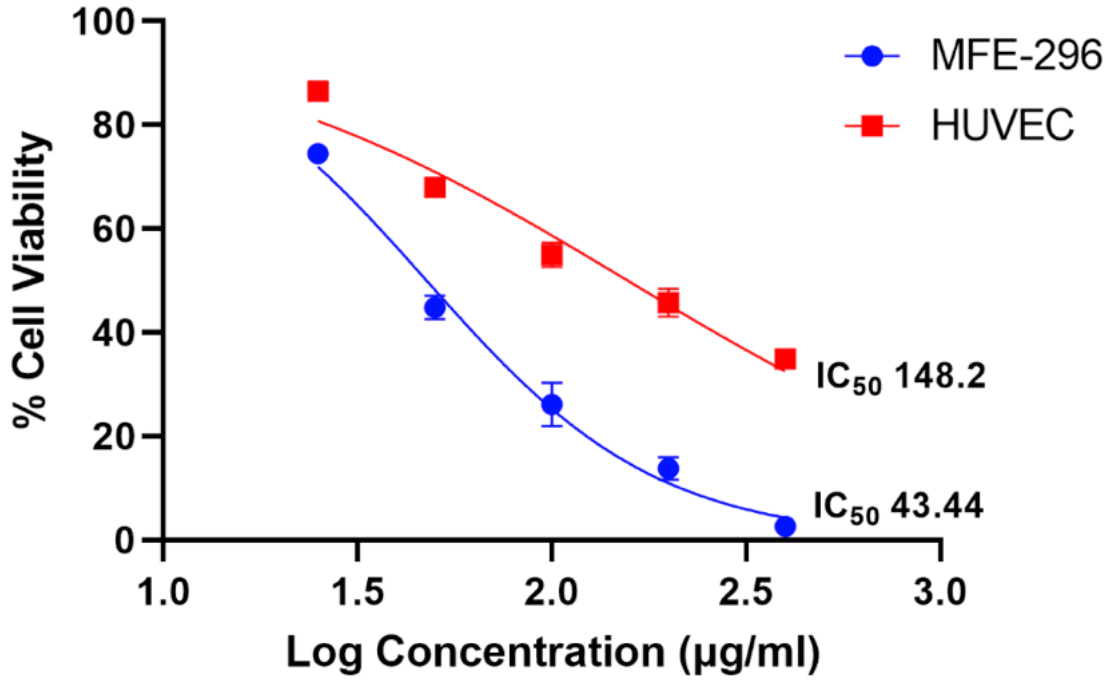

Figure 25

IC_{50} for Au(III)-Complex in (MFE-296) cell line and (HUVEC) natural cell line.

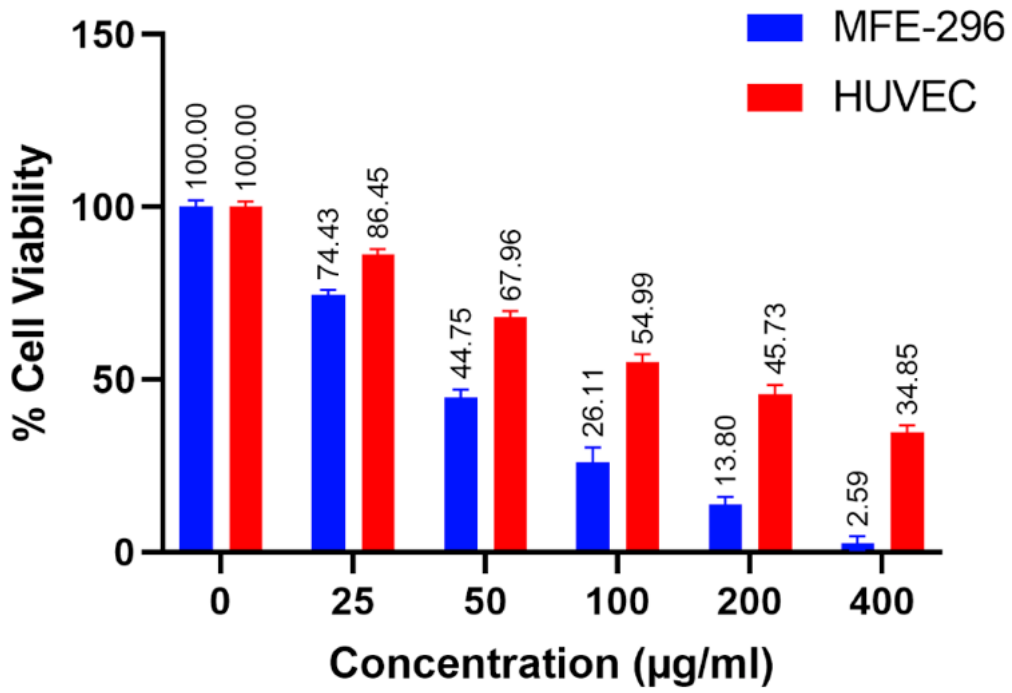

Figure 26

For Au(III)-Complex % viability, a comparison was made between carcinoma and natural cells

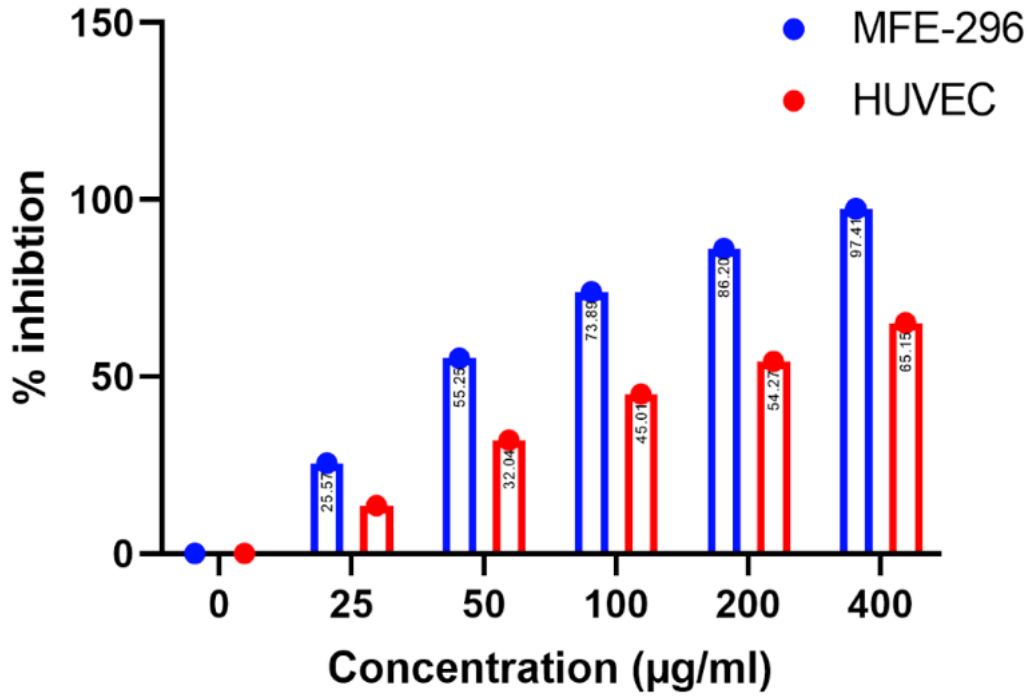

Figure 27

For Au(III)-Complex % inhibition, a comparison was made between carcinoma and natural cells.

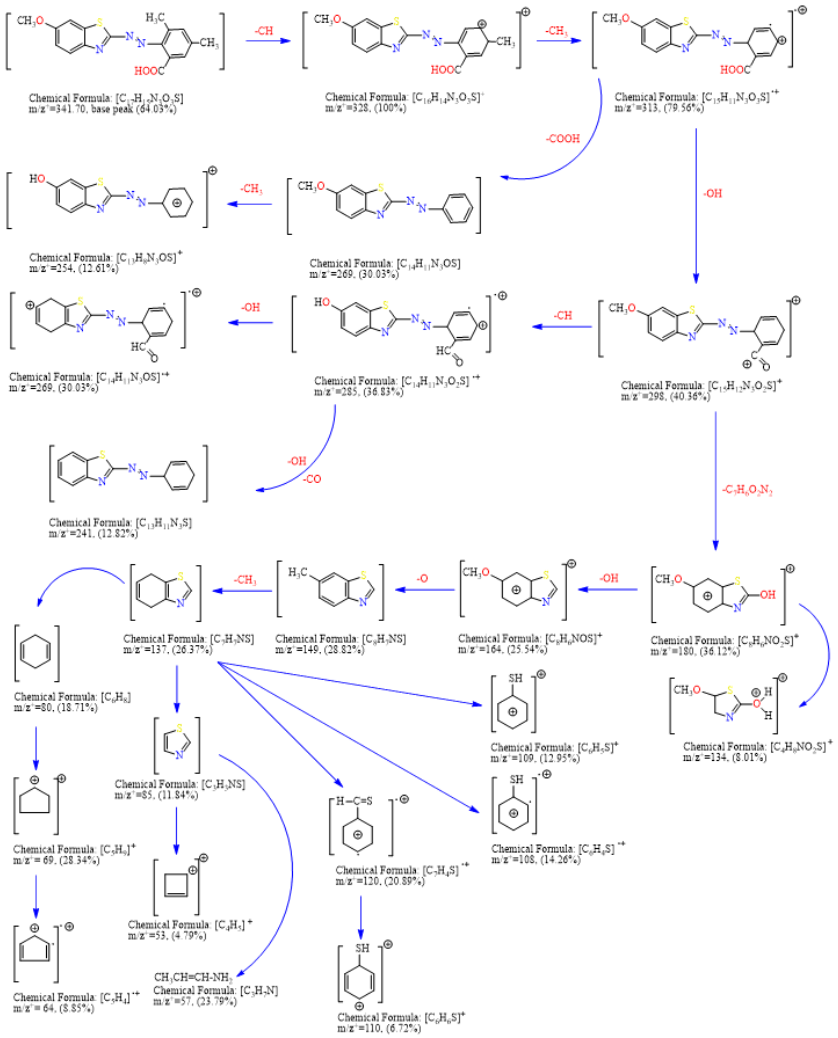

Figure 28

Scheme 1. Mass spectrum fragmentation of (6-MBTAMB)

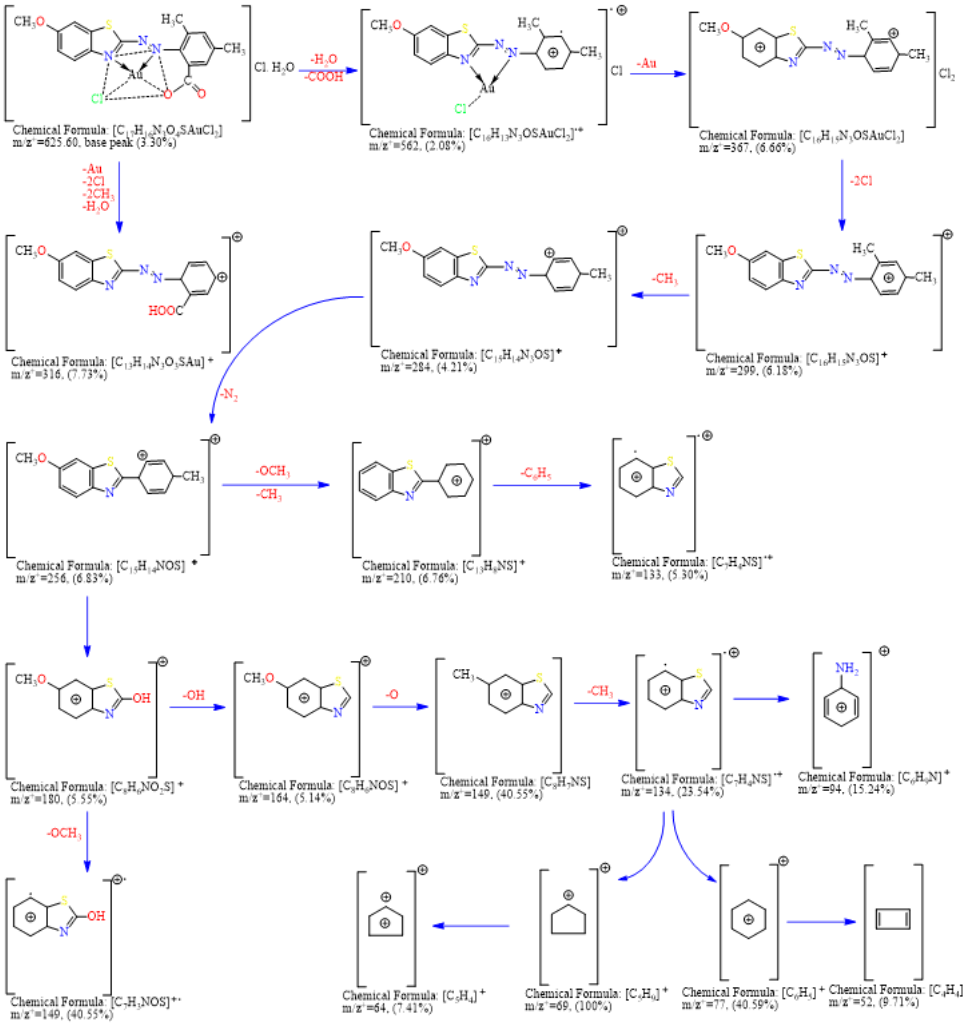

Figure 29

Scheme 2. Mass spectrum fragmentation of Au(III)-Complex.

Supplementary Files

This is a list of supplementary files associated with this preprint. Click to download.

- floatimage53.png